Hydrodynamic effects of leading-edge tubercles on control surfaces and in flapping foil propulsion.

by

Michael Jordan Stanway

B.S., Ocean Engineering
Massachusetts Institute of Technology (2006)

Submitted to the Department of Mechanical Engineering
in partial fulfillment of the requirements for the degree of

Master of Science in Ocean Engineering

at the

MASSACHUSETTS INSTITUTE OF TECHNOLOGY

February 2008

Author .....
Department of Mechanical Engineering
Center for Ocean Engineering
January 22, 2008

Certified by .....
Alexandra H. Techet
Associate Professor of Mechanical and Ocean Engineering
Thesis Supervisor

Accepted by .....
Lallit Anand, Professor of Mechanical Engineering
Chairman, Department Committee on Graduate Students

Hydrodynamic effects of leading-edge tubercles on control surfaces and in flapping foil propulsion.

by

Michael Jordan Stanway

Submitted to the Department of Mechanical Engineering
on January 22, 2008, in partial fulfillment of the
requirements for the degree of
Master of Science in Ocean Engineering

Abstract

This thesis investigates the hydrodynamic effects of biologically-inspired leading-edge tubercles. Two complementary studies examine the performance of three-dimensional hydrofoils based on the pectoral flippers of the Humpback Whale (*novangilae megaptera*). The first study uses a static foil, with application to conventional control surfaces– such as rudders or dive planes–found on marine vehicles. The second study uses a dynamic foil, with application to flapping foil propulsion.

The lift and drag characteristics of foils with and without tubercles are compared using force measurements from experiments conducted in a water tunnel at four Reynolds numbers between 4.4×10^4 and 1.2×10^5. Results from these experiments indicate the foils stall from the trailing edge in the range of Reynolds numbers tested. Stall was delayed on the foil with tubercles; maximum lift was reduced in all cases but the highest R_e. PIV flow visualization at $R_e = 8.9 \times 10^4$ showed flow separation at the trailing edge of both foils as attack angle was increased, confirming that the foils were in trailing edge stall. Surface normal vorticity in ensemble averaged flow fields showed distinct pairs of opposite sign vortical structures being generated by the tubercles, providing some insight into the fluid dynamic mechanism that leads to changes in the performance of a foil with tubercles.

Tubercles were used on a flapping foil for the first time. Mean thrust coefficient, C_T, power coefficient, C_P, and efficiency, η, were measured over a wide parametric space. The maximum thrust coefficient and efficiency measured using the smooth control foil were $C_T = 3.511$ and $\eta = 0.678$. The maxima using the tubercled test foil were $C_T = 3.366$ and $\eta = 0.663$. In general, the foil with tubercles performed worse than the control, and this performance deficit grew with increased loading. These results suggest that the vortical structures generated by the tubercles interfere with the thrust wake generated by flapping, ultimately degrading performance.

Thesis Supervisor: Alexandra H. Techet
Title: Associate Professor of Mechanical and Ocean Engineering

Acknowledgments

I would like to thank all of the people that have supported me during my time here at MIT. My advisor, Prof. Alexandra Techet, provided support and encouragement in this project from the time I started it as a UROP. Prof. Franz Hover and Stephen Licht were invaluable in my troubleshooting efforts, which seemed at times to be my only efforts. My EHL labmates, Tadd Truscott, Vera Pavel, Brenden Epps, and Jesse Belden asked the right questions and helped me clarify my thoughts, I hope I've been able to do the same for them in their projects. Tadd, Jason Dahl, and Dr. Rich Kimball introduced me to the proper care and feeding of the water tunnel. Rick Amaral and Bob Strong worked long and hard to make sure we didn't blow up the lab when we were transitioning to the new tunnel controls. I'd also like to thank the tunnel for behaving so well once we got those controls working.

I'd also like to recognize some groups that gave me experiences and tools I used in this research. Prof. Frank Fish of West Chester University provided the original foil models. Prof. Tom Consi (now at University of Wisconsin) helped me get my feet wet with my first undergraduate research project and taught me the importance of keeping a good lab notebook. Prof. Michael Triantafyllou, Prof. Chrys Chryssostomidis, and Christiaan Adams, helped me continue the Discover Ocean Engineering FPOP and taught the undergrad OE capstone design class in 2005 with Franz. I'd like to thank my classmates in that project, the echolocators, for their collaboration and teamwork. I learned a lot from them and also from the MIT ROV Team these past few years. I'd like to recognize Fred Cote and the Edgerton Machine Shop, for giving me the machining skills I've used in this project and so many others.

I am grateful for the financial support I have received, as scholarships and fellowships, from the Center for Ocean Engineering, the Department of Mechanical Engineering, the Society of Naval Architects and Marine Engineers, the American Society of Naval Engineers, the American Bureau of Shipping, and most recently the American Society for Engineering Education.

To all the 13SEAS officers and members, past, present, and future, and to all the members of the Center for Ocean Engineering, I thank you for helping keep Ocean Engineering alive at MIT.

Finally, I'd like to thank my family for the support they've given. Without you, I wouldn't have gotten here in the first place, and I certainly wouldn't be headed wherever it is that I'm going.

...by the way, does anyone know where that is?

Contents

List of Figures

List of Tables

Chapter 1

Introduction

The first goal of any biomimetic study is to understand the physics of a biological solution to a particular problem. The second goal is to distill that understanding to its essential components, allowing an engineer to apply the most important principles to a man-made solution. In this sense, biomimetics is really a misnomer–the researcher does not seek to mimic nature's solution, but instead to draw inspiration and understanding from it. This thesis consists of two separate but complementary studies on a biologically-inspired design: leading edge tubercles.

Tubercles are perturbations, or bumps, on the leading edge of the pectoral flippers of a humpback whale (*Megaptera novæangilæ*), shown in Figure 1-1. These animals depend on maneuverability to survive, and one of the reasons they are so maneuverable is the unique hydrodynamic design of their pectoral flippers. The studies presented in this thesis use two experimental hydrofoils modeled after these flippers. One has sinusoidal perturbations to the leading edge that are meant to simulate tubercles. The other has a smooth leading edge and provides a baseline for comparison. The first study investigates the effects of tubercles on a static foil, like a conventional control surface on a marine vehicle. The second study applies tubercles to a dynamic foil–one used in flapping foil propulsion.

Figure 1-1
Photographs of a humpback whale breaching in the Southern Ocean and a closeup of its pectoral flipper. Note the prominent tubercles on the leading edge.

1.1 *Megaptera novæangilæ*

The humpback has the largest pectoral flippers of any whale [25]. In fact, its latin name, *Megaptera novæangilæ*, translates to "giant wings of new england." Its flukes and flippers are even larger than those of the Blue whale (*Balænoptera musculus*), the largest animal ever to have lived on this planet. Adult humpbacks grow 11-15 meters in length and weigh 32,000 kg on average. They are a migratory species ranging from feeding grounds in cold polar waters to calving grounds in warm waters near the equator. Whale watching has made humpbacks well-known for their spectacular acrobatic displays and haunting song.

Despite their size, they are highly maneuverable predators with several different specialized modes of capturing their prey. They feed primarily on schools of plankton, euphasiids, herring, and capelin [5]. When prey is abundant, the whale will swim through the school from below at a typical speed of 2.6 m/s (5 kts). This lunge-feeding behavior is also used with lateral or inverted approaches [11]. The whale will sometimes swim away from its prey and quickly reverse direction with a U-turn before lunging back through the school. This "inside loop" behavior can be completed in as little as 1.5 body lengths [8]. Flick-feeding is another behavior that requires rapid, tight turning capability. The whale begins a dive with its flukes clear of the water,

flicks its tail as it submerges, and lunges to the surface with its mouth open to the resulting food-filled wave [11]. Bubblenetting is perhaps the most intriguing feeding behavior of the humpback whale. Swimming upward in a spiral, the whale blows bubbles in a ring that concentrates its prey in the center. The whale then lunges from below with an open mouth, engulfing its prey. These nets range from 1.5 m to 50 m in diameter, depending on the prey. Cooperative bubblenetting by multiple whales has often been observed, often in conjunction with singing [11].

A high degree of agility, lacking in other baleen species, is required in each of these behaviors. A humpback would go hungry if it could not maneuver well; this encourages a hydrodynamically specialized evolutionary pathway different from other species of whale.

Fukes and flippers contribute to the humpback's maneuverability in different ways. The large planform area and relatively low aspect ratio of the flukes allow the whale to accelerate quickly [25] and its highly flexible tail allows it to vector initial accelerations effectively [4]. While the whale beats these flukes to propel itself through the water at high speeds, the pectoral flippers serve as highly effective hydroplanes that allow the whale to roll, somersault, and execute tight banked turns. When there is little flow over the flippers to produce maneuvering forces, sculling and rowing motions have been observed. Swimming in this manner is restricted to low speeds, but can lead to movement in virtually any direction [4].

These magnificent mammals have evolved through millenia of selective pressure. They have adapted to life in their fluid element, and tubercles seem to be a unique part of that adaptation. The studies in this thesis aim to provide a better understanding of what tubercles do and how they do it.

1.2 Outline of the Thesis

The application of tubercles to a conventional control surfaces is investigated in the static foil study comprising Chapter Two. The study begins with a review of previous research on humpback whale flippers, and specifically the fluid dynamic effect of

tubercles. The performance metrics for a control surface are then defined, and stall is introduced as the principal performance limitation. Force measurements are used to evaluate and compare the lift and drag characteristics of the smooth control foil and the tubercled test foil. The flow over the planform surface of the foil is measured using Particle image velocimetry (PIV) for the first time in an effort to understand the fluid dynamic mechanism tubercles use to modify performance of the static foil.

Chapter Three shifts the focus from conventional control surfaces to flapping foil propulsion. This topic has been studied extensively using analytical, numerical, and experimental techniques, with the hope of engineering a propulsor that can enhance maneuverability while maintaining high efficiency for cruising. This study is the first time tubercles have been used on a flapping foil. It begins by introducing the kinematics and principal dimensionless parameters of flapping. Several performance metrics are defined which will be used to compare results from different flapping parameters and different foils. A literature review then summarizes previous studies using both two-dimensional and three-dimensional flapping kinematics. Experimental apparatus and procedures are introduced using force data from one test. Thrust, power, and efficiency measurements over a wide parametric range are presented and the performance characteristics of both foils are compared. Another set of experiments compares the lift and thrust generating capabilities of both foils for use in maneuvering.

Key points from both studies are summarized in Chapter Four. Recommendations are made regarding the use of tubercles on control surfaces and flapping foils, and suggestions for future research are given.

Further details on the experimental results and particulars of the experimental setup can be found in the appendices.

Chapter 2

Static Foil Study

2.1 Introduction

Control surface performance is an important aspect of vehicle design in ocean and aeronautical engineering. It dictates how maneuverable a vehicle is and how efficiently it can move through a fluid. Studying nature's solutions to these problems can provide insight and inspiration that allows engineers to improve man-made designs. The Humpback Whale is one source of this biological inspiration. It is a highly maneuverable animal, despite its size, and much of its acrobatic prowess is attributed to the use of its unique pectoral flippers as specialized control surfaces.

2.1.1 Pectoral flipper morphology and function

The pectoral flippers of the humpback are the largest found on any whale, both in relative and absolute size, averaging 30.8% of the whale's total body length [25]. The high aspect ratio and backswept elliptical planform shape provide an efficient lifting surface. The streamlined cross-section is consistent with engineered subsonic foil sections of a 20% thickness ratio [5]. Perhaps the most notable feature of the flipper is the scalloped leading edge. Protuberances, called tubercles, on the outboard two-thirds of the flipper are a functional adaptation that enhances maneuverability.

The humpback has the most energetically demanding feeding behaviors of any

baleen whale. Its prey is quick and agile, so the humpback has to employ maneuvers such as loops, barrel rolls, and tight, fast turns in order to survive [11, 25]. It is well known that leading edge modifications affect the performance of a foil, and several researchers have suggested that tubercles are a hydrodynamic adaptation to improve maneuverability.

An important consideration in any biologically-inspired study is that animals evolve in response to many selection pressures. Some of these pressures are directly opposed, and it is unlikely that a particular behavior or morphological feature is a response to just one of these pressures. In the case of humpback whales, thermoregulation is another pressure, aside from maneuverability, that probably contributed to the development of tubercles. The humpback migrates yearly from cold feeding grounds in the arctic and antarctic to warmer equatorial waters for mating and calving. Researchers have acknowledged that the pectoral flipper itself serves a thermoregulatory function [4]. The large surface area and vascular tissue in the flipper support this, and it is possible that tubercles further enhance heat exchange by improving mixing over the flipper.

This study recognizes the thermoregulatory function of tubercles, but focuses on their part in enhancing maneuverability. The underlying physical mechanisms are investigated using measurements of the forces on a foil with tubercles and the further measurements of the flow over it.

2.1.2 Performance metrics for a control surface

A control surface on a vehicle moving through a fluid can be represented by a static foil oriented with some attack angle, α, to a flow. It produces a useful force normal to the flow, defined as lift, and a parasitic force aligned with the flow, defined as drag. In a right-handed coordinate system with the x-axis oriented to the flow, $D = X_0$ and $L = Y_0$, as shown in Figure 2-1. In general, these forces are a function of the fluid density, ρ, flow velocity, U, mean chord, $\bar{c}$, and span, b . They are nondimensionalized

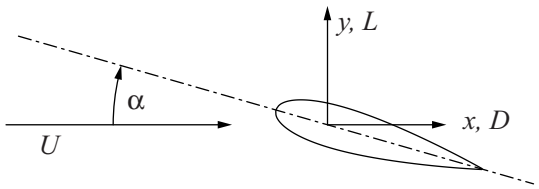

Figure 2-1
Definition of coordinate system and forces for a foil with attack angle α in a fluid with velocity U. x, y, z is a right-handed coordinate system with x aligned to the flow. Drag is positive in x and lift is positive in y.

as the lift coefficient:

$$C_L = \frac{Y_0}{\frac{1}{2}\rho U^2 \bar{c} b}, \tag{2.1}$$

and the drag coefficient:

$$C_D = \frac{X_0}{\frac{1}{2}\rho U^2 \bar{c} b}, \tag{2.2}$$

which are measured as a function of the attack angle. The lifting efficiency can be described by the lift-to-drag ratio. Performance can also be dependent on the Reynolds number, $R_e = (U\bar{c})/\nu$, which represents the ratio of inertial to viscous forces. This study compares C_L and C_D of both foils over a range of α for several R_e.

2.1.3 Mechanism of stall

The principal performance limitation of a control surface is stall. This is the loss of lift as attack angle is increased beyond a critical value and flow separates either at the leading or trailing edge. Stall type is dependent on cross-section shape, thickness ratio, and Reynolds number [9]. Laminar leading edge separation produces long-bubble stall, where the flow reattaches to the foil further downstream. The separation bubble grows with lift coefficient, until it reaches the trailing edge and the flow becomes fully detached. This type of stall is characteristic of very thin sections and those with sharp leading edges operating in laminar flow. In short-bubble stall, the separation bubble actually shrinks with increasing attack angle. Lift coefficient continues to increase linearly with attack angle until a point where the bubble bursts, resulting in complete separation and an immediate loss of lift. This type of stall is most typical in thin sec-

tions with round leading edges. Sections with increased thickness or camber tend to stall at the trailing edge rather than the leading edge. The boundary layer grows and separates from the foil, but does not reattach. The detachment point moves toward the leading edge as stall progresses, finally transitioning to fully detached flow. This type of stall is characterized by a gentle loss of lift with increasing attack angle. For further information on these stall types and their characteristics, refer to Hoerner [9].

2.1.4 Previous Studies

Fish and Battle [5] suggest tubercles generate vortices to maintain lift and delay stall. Fish and Watts [24] employ a three-dimensional panel method code to investigate a rectangular wing with and without tubercles, they find an increase in lift and a reduction in induced drag. They suggest the reduction in induced drag is due to the troughs acting as fences and reducing tip vortices. Miklosovic, et. al. [17] demonstrate increased lift and delayed stall on a three-dimensional idealized humpback flipper in a wind tunnel at $R_e \simeq 5 \times 10^5$. This work is extended in [19] to include sweep angles of 15° and 30° with similar results. Levshin, et. al. [12] investigated the effect of tubercle frequency and amplitude on a two-dimensional rectangular foil at $R_e = 1.83 \times 10^5$. Pre-stall lift was decreased by the presence of tubercles, but post-stall lift was increased. This effect was more pronounced with higher amplitude tubercles, but independent of tubercle frequency. Miklosovic, et. al. [18] also included experiments on a full-span rectangular wing; lift was decreased and and drag was increased in the two-dimensional case, while the opposite occurred for the three-dimensional wing. This suggests that tubercle effects may be coupled with planform shape and Reynolds number effects.

2.2 Experimental Setup

Two hydrofoils were designed for these experiments (Figure 2-2) so that they share all major dimensions, including planform area. The test foil features idealized leading edge tubercles. The elliptical planform is swept back to match the shape of a hump-

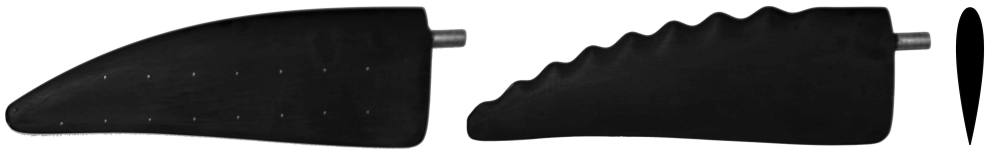

Figure 2-2
Photograph of the two experimental hydrofoils. The control foil is on the left and the test foil is on the right. Both have a NACA 0020 cross section and are identical in all major dimensions, including planform area. The test foil features a sinusoidal leading edge meant to emulate the tubercles found on the Humpback Whale (*Megaptera novæangilæ*).

back flipper. The foils have a NACA 0020 cross-section, a mean chord of $\bar{c} = 5.95$ cm and a span of $b = 24.6$ cm. The geometric aspect ratio of the foils is $\mathcal{AR} = 4.132$.

The foils are modified versions of those used by Miklosovic, et. al. in [17], which were based on the left pectoral flipper of a 9.02 m male humpback. The foils in this study are scaled down and material has been removed at the root so that they fit on the experimental apparatus. Frank E. Fish, of Westchester University, provided CNC-milled polycarbonate models that were used to make molds of Silicone RTV (McMaster 8595K65). The experimental foils were then cast using a low-viscosity urethane (McMaster 87075K57) poured onto a type 6061 aluminum skeleton. They are painted matte black to reduce laser reflections that would affect the PIV data, and then sanded with progressively finer sandpaper down to 600 grit to provide a smooth surface finish.

Experiments were conducted in the recirculating water tunnel in the Marine Hydrodynamics Laboratory at MIT, shown in Figure 2-3. The 56 kW main motor drives an impeller capable of producing freestream velocities up to 8 m/s. Turbulence is minimized by flow straighteners, a honeycomb mesh, and a 5:1 contraction upstream from the test section. Experiments are installed and accessed through four 0.51 m by 1.5 m plexiglas windows comprising the walls of the test section. Equipment in this thesis was installed in the top window with a free-flooding aluminum offset box and thermoformed ABS fairing. Freestream velocity is measured upstream of the foil at the center of the tunnel using laser doppler velocimetry. Experiments discussed here were performed at velocities of 0.75, 1.00, 1.50, and 2.00 m/s, corresponding to R_e between 4.4×10^4 and 1.2×10^5.

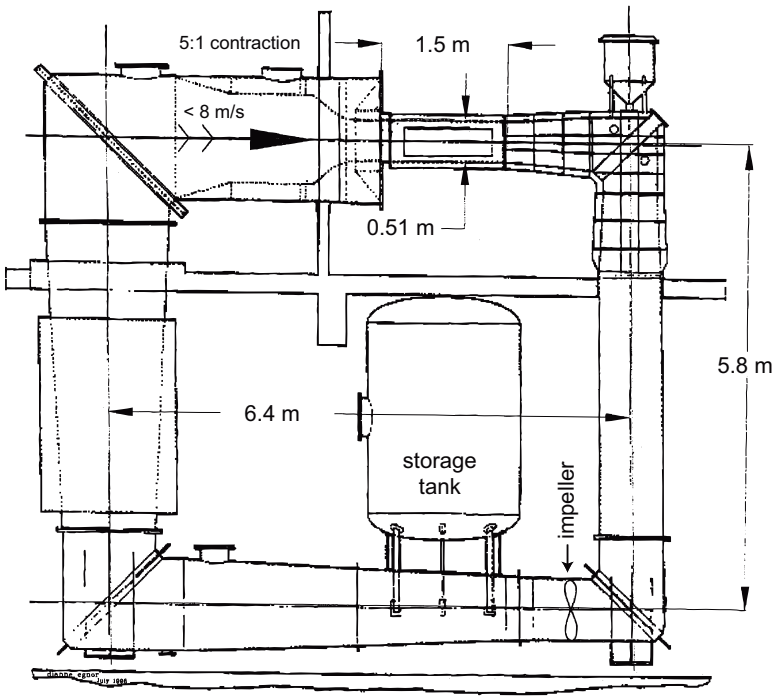

Figure 2-3
Schematic of the recirculating water tunnel in the Marine Hydrodynamics Laboratory at MIT.

A six-axis submersible dynamometer (Advanced Mechanical Technology, Inc. MC1-6-250) mounted to the root of the foil measures forces and moments. It uses a six full-bridge strain gauges oriented to provide the total force vector, $\boldsymbol{X}_s$, in sensor-referenced x, y, and z coordinates. Only forces in the xy-plane will be discussed here. The sensor is potted in urethane for waterproofing. It is inherently pressure compensated because both the inner and outer diameters of the strain element are exposed to ambient pressure, providing a net differential of zero.

An external power supply provides a common 10 VDC excitation to all six channels. It is continuously monitored and maintained within 0.01 VDC. The microvolt level sensor outputs are amplified and conditioned by a universal strain gauge input module (National Instruments, SCXI-1520) with a 100 Hz analog four-pole butterworth low-pass filter. All signals are recorded at 500 Hz by a 16-bit multifunction data acquisition card (National Instruments, PXI-6031E).

The foil is rotated using a 48 VDC servomotor (Moog Components Group, Type C13G). Angular position is monitored by a potentiometer (Inscale Measurement Tech-

nology Ltd., GL200) mounted to the shaft to remove effects from backlash in the gearhead and drivetrain. The potentiometer is powered and conditioned by an isolation amplifier (National Instruments SCXI-1121) and recorded by the same data acquisition card as the dynamometer.

The dynamometer rotates with the foil, so it does not measure lab-referenced forces directly. There is also a small angular misalignment, ϵ between the foil and sensor coordinates. This misalignment is determined during calibration procedures each time the foil is mounted. (See Appendix A.2.2 for more details.)Sensor-referenced forces must undergo an angular coordinate transformation to be expressed in the lab frame.

$$\begin{Bmatrix} X_0 \\ Y_0 \end{Bmatrix} = \begin{bmatrix} \cos(\alpha+\epsilon) & -\sin(\alpha+\epsilon) \\ \sin(\alpha+\epsilon) & \cos(\alpha+\epsilon) \end{bmatrix} \begin{Bmatrix} X_s \\ Y_s \end{Bmatrix} \tag{2.3}$$

Major sensitivity values along the primary sensor axes were confirmed in lab. The dynamometer has a small amount of crosstalk between channels and this must be accounted for in calibration and converting the measurement voltages to corresponding forces and moments. The factory-supplied calibration data shows less than 2% crosstalk on all channels. This data provides a 6×6 sensitivity matrix, $\bar{\boldsymbol{S}}$, that uses a least squares fit and includes off-diagonal terms to account for crosstalk. A simple matrix inversion converts measured voltages to corresponding sensor-referenced forces.

$$\boldsymbol{X}_s = \bar{\boldsymbol{S}}^{-1}\boldsymbol{V} \tag{2.4}$$

2.3 Results and Discussion

2.3.1 Control foil

Force measurements for the smooth foil are presented in Figure 2-4. The lift coefficent of the smooth foil increases linearly up to $\alpha = 12^\circ$ with a slope of $dC_L/d\alpha = 0.069$. At attack angles greater than 12° the lift curve is no longer linear, flow separation near the tip of the foil causes partial stall. This mechanism is Reynolds-number dependent,

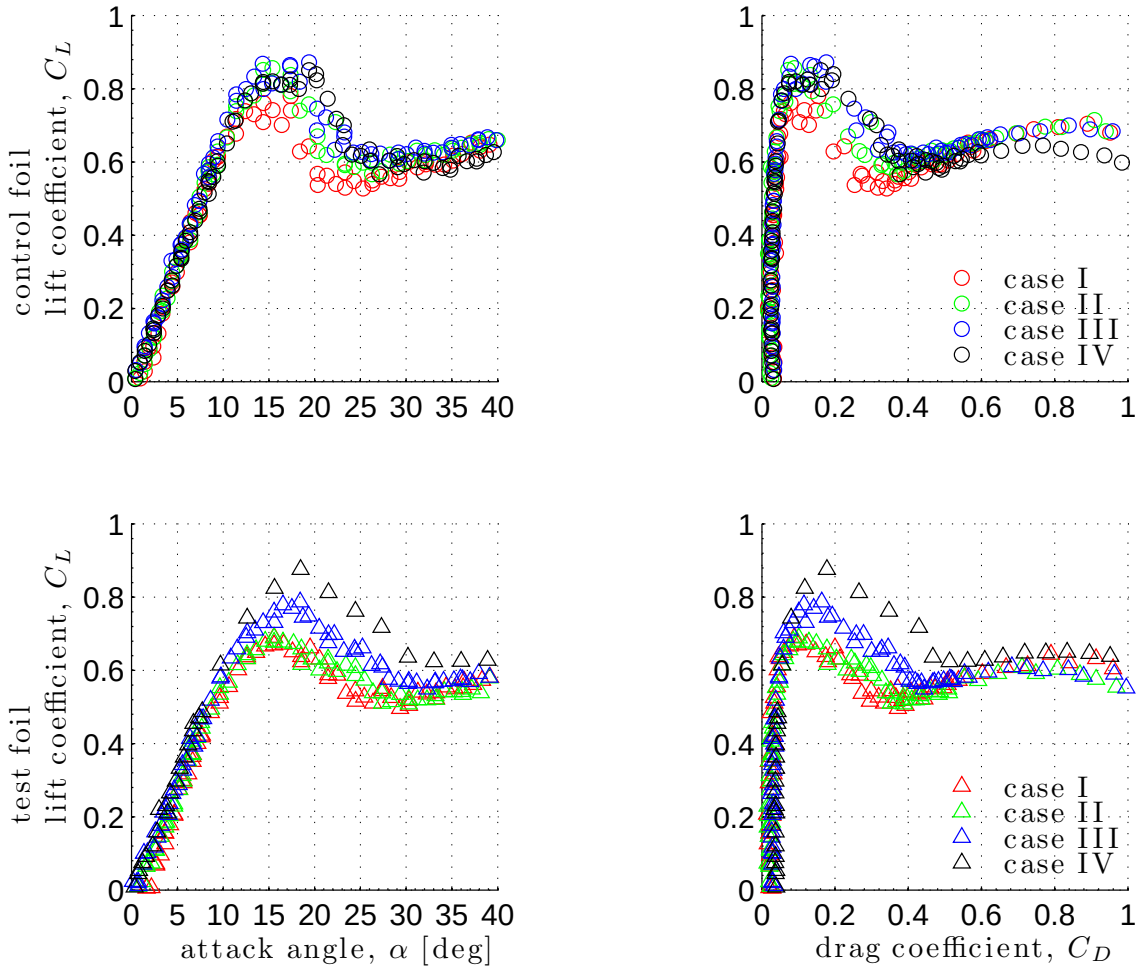

Figure 2-4
Force measurement results for smooth control foil (○) and tubercled test foil (△), presented as lift curves and drag polars. Reynolds numbers for each case were: case I: 44648, case II: 59530, case III: 89295, case IV: 119060

as evidenced by the spread between lift curves of different cases. In fact, the curve for case I changes slope earlier than the others, at $\alpha = 10°$. Higher R_e maintain lift better than lower R_e, indicating less viscous separation at higher speeds, as should be expected. Partial stall progresses into full stall at about 12° for the lowest R_e and about 19° for the highest. Beyond this, total lift decreases gradually in a manner consistent with trailing edge stall. The flow separates completely at $\alpha \simeq 30°$, and lift is no longer due to circulation, but to form drag. The drag polar for this foil shows a wide range of operating lift coefficients with low drag penalty. The lifting efficiency, $\eta_L = C_L/C_D$ at any operating point is the slope from the origin to that point. It is high for $C_D < 0.2$, but drops off quickly afterward.

2.3.2 Test foil

The lift curve of the tubercled foil, shown in Figure 2-4, is linear for $\alpha < 8°$ in cases I and II, and $\alpha < 10°$ in cases III and IV. The slope is $dC_L/d\alpha = 0.065$, 5.8% lower than that of the smooth foil. Here, the different Reynolds number tests diverge slightly and the slope decreases but remains linear. The secondary slope for case I decreases 44% to $dC_L/d\alpha = 0.039$ until $\alpha = 13.5°$, while for case IV it decreases 54% to $dC_L/d\alpha = 0.030$, but extends until $\alpha = 18.5°$.

Full stall begins at 15.5° for the lower two Reynolds numbers, but is delayed further to 18.5° in the higher Reynolds number tests. Loss of lift is shallow and predominantly linear, with $dC_L/d\alpha = -0.014$ for case I and $dC_L/d\alpha = -0.020$ for case IV. At $\alpha \simeq 30°$, the flow is completely separated and lift is again dominated by a component of pressure drag, but the highest R_e case maintains more lift than the others. Maximum lift is reduced from the test foil in all cases but IV. The test foil drag polar shows that the range of operating lift coefficients with low drag penalty is slightly reduced from the control foil, which is consistent with the reduction of maximum lift.

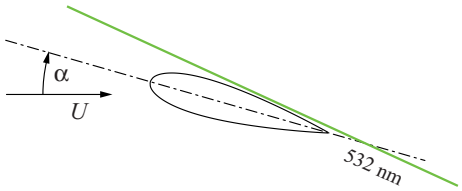

Figure 2-5
Experimental setup of the PIV experiments. The light sheet was rotated with the foil for each attack angle to maintain a consistent sample plane relative to the foil, but the light sheet and foil were not coupled by the experimental apparatus.

2.4 Flow Visualization

The flow over the suction side of the foil is imaged using PIV. The light sheet from a 532 nm Nd:YAG laser (New Wave Research, Tempest) illuminates reflective particles moving with the flow in a plane near the surface of the foil. A CCD camera (Megaplus Camera, Model ES 4.0) acquires timed image pairs 15 μs apart. DaVis post-processing software (LaVision GmbH) cross-correlates the image pairs to determine the velocity field in the illuminated plane. Results presented here are an ensemble average of 40 instantaneous velocity fields for each attack angle. The light sheet was rotated with the foil for each attack angle to maintain a consistent sample plane relative to the foil, but the light sheet and foil were not coupled by the experimental apparatus. The freestream velocity for all PIV tests was $U = 1.5$ m/s, corresponding to case III ($R_e = 8.9 \times 10^4$) of the force measurements.

2.4.1 Velocity fields

The first quantity of interest is the velocity in the illuminated plane. Figure 2-6 compares the velocity fields of the two foils at three attack angles. With attack angle $\alpha = 10°$, the flow speeds up to 2.3 m/s over the mid-chord of both foils. It slows back to 1.5 m/s downstream of the control foil. Small spanwise fluctuations are present, but no net spanwise transport is apparent Small areas of lower velocity (1.2 m/s) are observed downstream of the troughs between tubercles on the test foil.

Increasing the attack angle to 14° produces a marked change in the flow field.

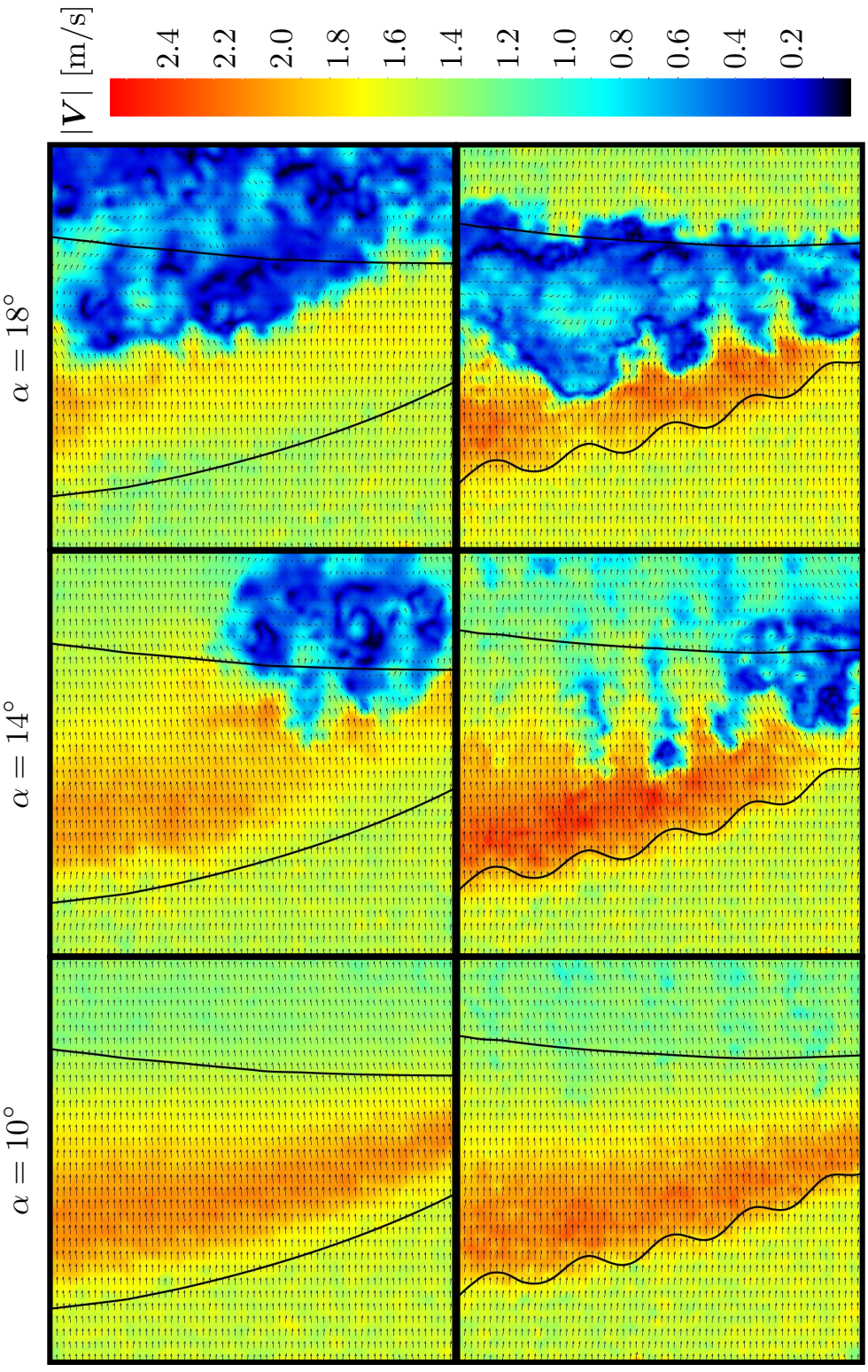

Figure 2-6
Comparison of representative instantaneous velocity fields at $\alpha = 10°, 14°, 18°$. Control foil is in the top row, and test foil in the bottom. Freestream velocity is 1.5 m/s (Case III, $R_e = 89295$). Areas in blue are low velocities indicating separation and stall.

The top half of the control foil maintains high velocities indicating the flow is still attached. The lower half of the foil has a large turbulent region of low velocity near the trailing edge, indicating that flow has separated. This trailing edge stall region is consistent with the gentle stall slope observed in the force data. The velocity field over the test foil shows even more change. Several low velocity cells appear downstream from the troughs. They are larger on the outboard part of the foil, but present even toward the root. A few pockets of very high (> 2.4 m/s) velocity are observed directly downstream of the troughs, before the low velocity cells appear. Significant spanwise velocities are present, but are balanced by opposite sign. Again there is no net transport toward either the root or the tip of the foil. The cells appear to decrease the area of the test foil still in attached flow. This is consistent with the presence of the secondary linear region in the lift curve. The cells also lend a degree of organization absent in the flow field over the control foil.

At $\alpha = 18°$, both foils are near maximum lift. Almost the entire rear half of the control foil is stalled, and its downstream flow is turbulent. The test foil, on the other hand, still shows organization in low velocity cells. These cells have grown and merged to form an almost complete stall region covering the downstream half of the foil. However, the beginnings of each cell are still apparent downstream of each trough. Something very interesting is happening in the area between the two upper troughs. The flow remains partially attached here, and will contribute to maintaining lift.

2.4.2 Chordwise vortical structures

The difference between the flows around the control and test foils becomes more apparent in the curl of the velocity field. This is the component of vorticity orthogonal to the illuminated plane:

$$\omega_z = \partial v/\partial x - \partial u/\partial y, \tag{2.5}$$

and will be referred to as the surface normal vorticity.

Instantaneous surface normal vorticity over the control foil shows random fluctu-

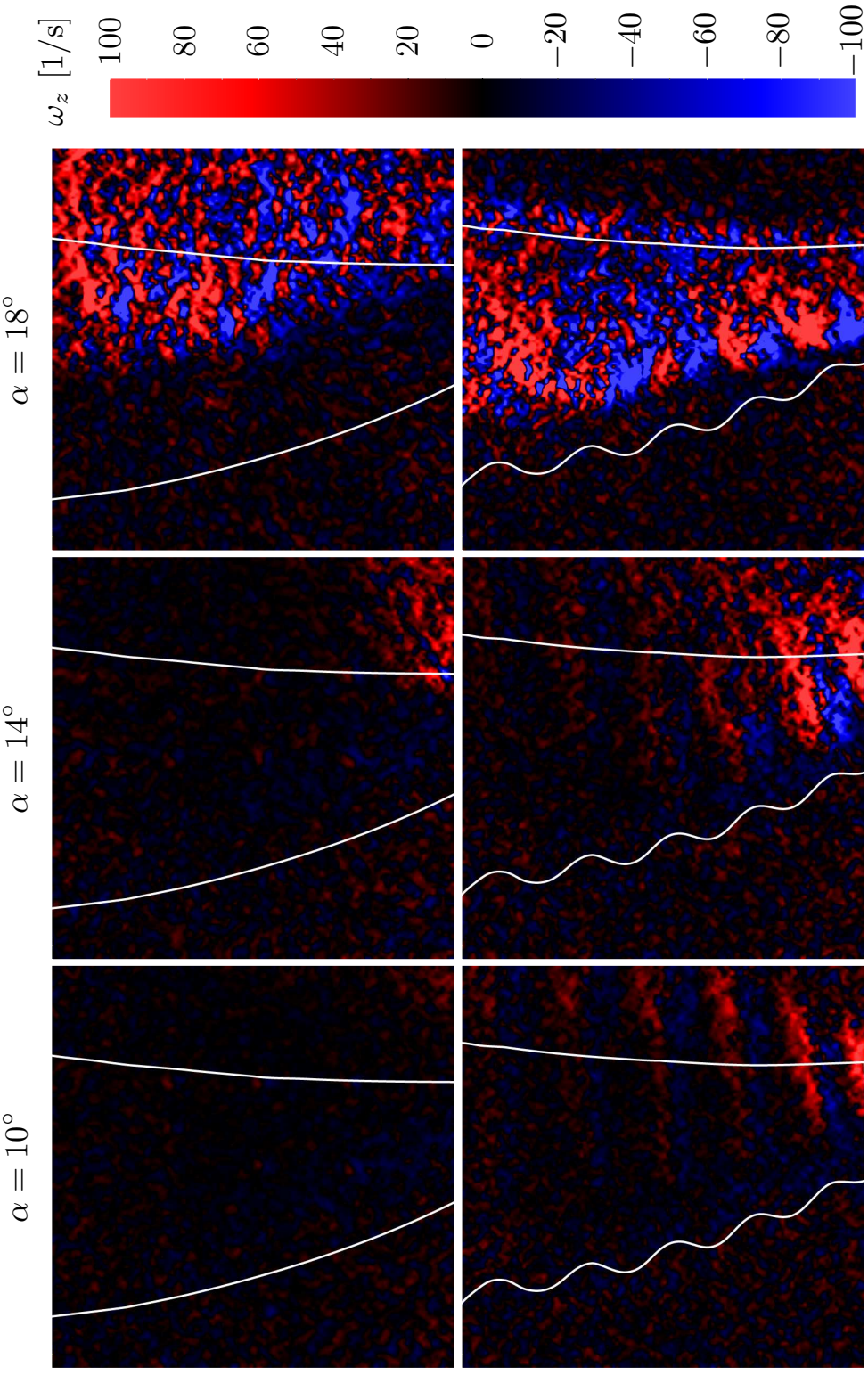

Figure 2-7
Surface normal vorticity, ω_z, in the ensemble average velocity fields at $\alpha = 10°, 14°, 18°$. Control foil is in the top row, and test foil in the bottom. Freestream velocity is 1.5 m/s (Case III, $R_e = 89295$). Note the pairs of vortical structures downstream from each tubercle.

ations in the flow over all attack angles. These fluctuations grow stronger as the flow separates and becomes more turbulent, but the ensemble average over 40 instantaneous fields (Figure 2-7) shows no evidence of organized structure.

The flow over the test foil, on the other hand, exhibits a high degree of organization. Chordwise vortical structures are apparent at $\alpha = 10°$. They appear in spanwise pairs of opposite sign downstream from each tubercle. Even just before complete stall, at $\alpha = 18°$, these structures persist. The flow over the test foil is much more organized here than the flow over the control foil.

Figure 2-8 shows the progression of these structures with attack angle from $\alpha = 10°$ to 20°. They strengthen with increasing α, and pairs appear to strengthen together. Structures near the foil tip are generally stronger than those near the root for a given attack angle. In some cases one pair is obliterated (e.g. the pair behind the second tubercle down in $\alpha = 18°$), but they always appear in pairs of similar strength and opposite sign.

These structures, while they do lend organization to the flow, are an unsteady phenomenon. The flow fields presented above are ensemble averages over 40 sample fields. The structure pairs fluctuate in strength with time, sometimes completely disappearing and reappearing.

2.5 Conclusions

The effect of tubercles depends on stall type, and is therefore sensitive to Reynolds number. Lift and drag measurements presented here show characteristics of trailing edge stall for both control and test foils. Maximum lift is lower for the test foil in all cases but IV, but stall is delayed and more gradual for the test foil in all cases. Miklosovic , et. al. [17] recorded increased maximum lift and delayed stall on similar three-dimensional foils at $R_e \simeq 5 \times 10^5$. Their measurements exhibited short-bubble type leading edge stall and the corresponding bubble-bursting immediate loss of lift.

It is reasonable to expect leading edge modifications, such as tubercles, to have marked effects on leading edge stall. This study, however, has shown similar effects

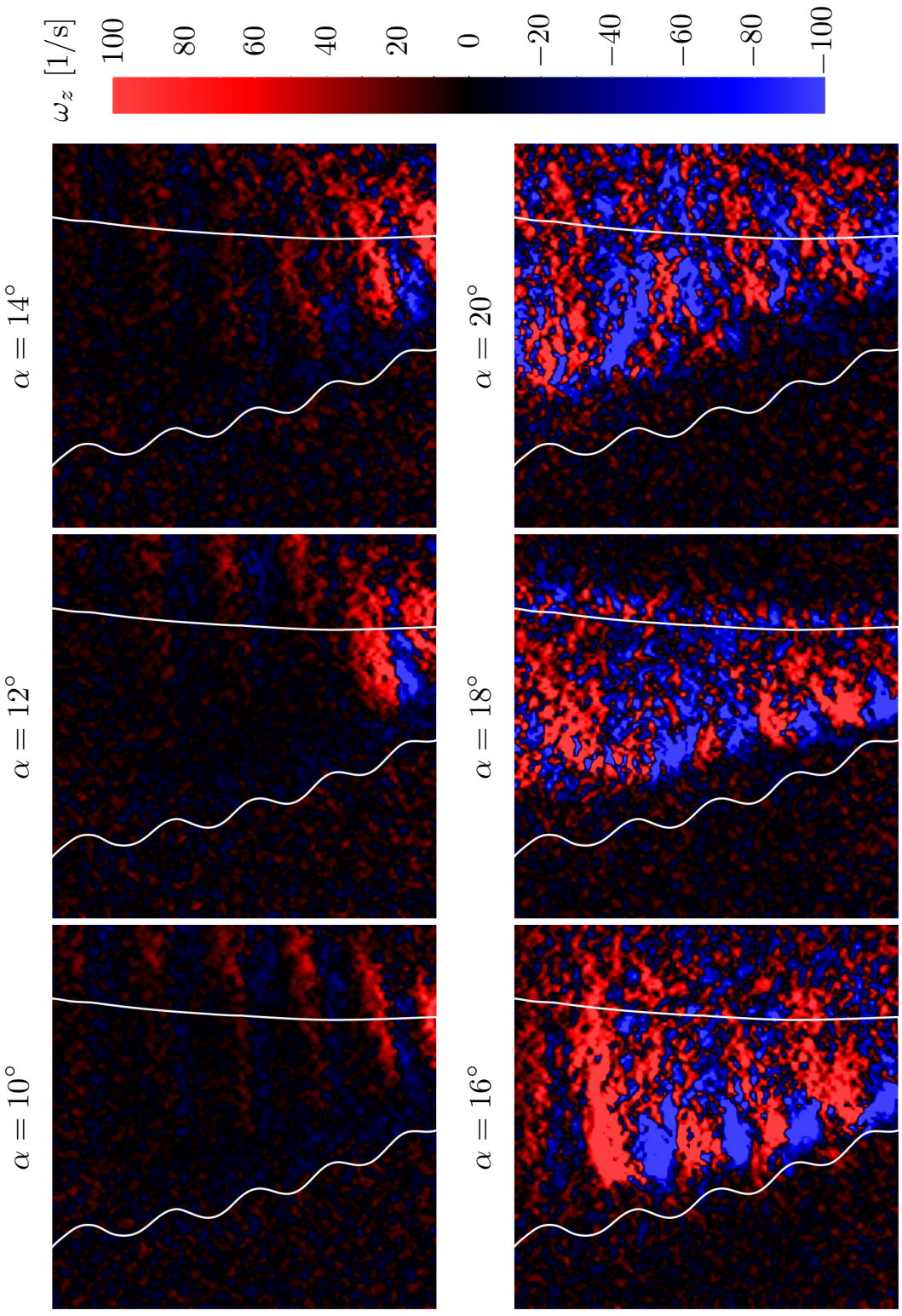

Figure 2-8
Surface normal vorticity, ω_{z_l}, in the ensemble average velocity fields over the tubercled test foil at $\alpha = 10° : 2° : 20°$. Freestream velocity is 1.5 m/s (Case III, $R_e = 89295$). Note the pairs of vortical structures increase in strength with attack angle.

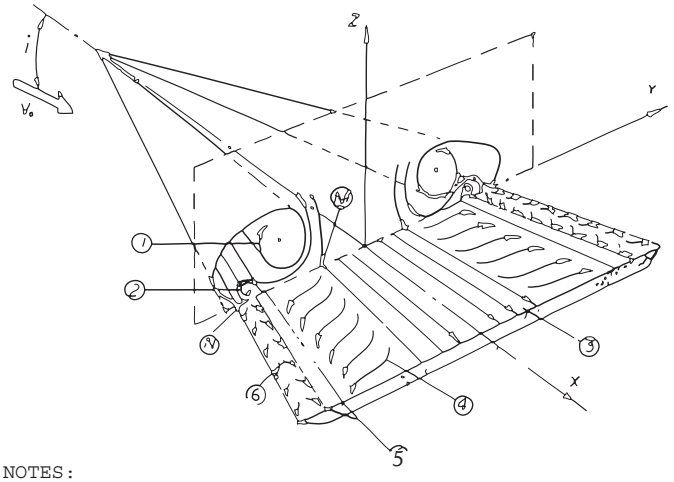

Figure 2-9
Schematic of flow over a delta wing by Hoerner [9]. Note the vortical structures rolling up off the leading edge of the wing and convected downstream.

are present with trailing edge stall. It has also provided insight into the mechanism that produces these effects, namely the chordwise vortical structures that organize the flow.

These structures may also act in a manner similar to the leading-edge vortices of a delta wing, shown schematically in Figure 2-9. The primary vortex rolls up off the leading edge and convects downstream above the surface of the wing. The suction force of this vortex produces lift even at high attack angles where normal high $\mathcal{R}$ foils would stall. It is possible that the surface normal vorticity measured in this study was due to a series of rolled-up leading edge vortices like this. PIV on a plane normal to the flow could confirm this, but was not possible with the current experimental setup.

The results of this study, coupled with those from previous studies, suggest that foils operating in a short bubble stall regime will benefit more from the addition of

tubercles than those operating in a trailing edge stall regime. Thinner foils operating at higher R_e are more likely to experience increased maximum lift, but stall will be delayed even for thicker foils at low R_e. It would be interesting to experiment with tubercles on thinner cross-sections, and on cambered foils where maximum lift is already increased by foil geometry.

Chapter 3

Dynamic Foil Study

3.1 Introduction

Fish and other aquatic animals move by controlling vorticity in the fluid surrounding them. They exhibit greater maneuverability than man-made marine vehicles, while at the same time maintaining high efficiency. The goal in studying flapping foils is to understand vorticity control and to use this understanding to engineer better marine robots. This study investigates the application of tubercles to flapping foil propulsion.

Flapping foils operate based on unsteady flow principles whereas conventional screw-type propellers are designed for predominantly steady flow. This often makes flapping foils more difficult to study and to design, but it also makes them ideal for maneuvering applications. Since flapping foils can produce large forces on short timescales, they are better suited to operating in dynamic environments like near-shore littoral zones.

Previous studies have investigated two types of flapping foil kinematics. A foil oscillating in heave and pitch presents a simple case of two-dimensional kinematics. This operates like the caudal fin of a fish or the flukes of a cetacean. In the case of simple harmonic flapping, the two coordinated motions are sinusoidal and share a common frequency, $\omega = 2\pi f$. The large-displacement motion is primarily linear (up

and down, in the case of a dolphin or whale, hence heave).

$$h(t) = h_0 \sin(\omega t) \tag{3.1}$$

The small motion is a feathering rotation around the spanwise axis of the foil (also up and down, in the case of a dolphin or whale, hence pitch). It follows heave by a constant phase angle, ψ. In general, it also has a constant bias angle, θ_{bias}. This is set to zero in the case of symmetric flapping used for pure thrust production, but it is important in generating maneuvering forces.

$$\theta(t) = \theta_0 \sin(\omega t - \psi) + \theta_{bias} \tag{3.2}$$

The second type of flapping foils operate more like a penguin wing or turtle flipper. These kinematics replace the large displacement linear motion (heave) with a large displacement rotational motion (roll).

$$\phi(t) = \phi_0 \sin(\omega t) + \phi_{bias} \tag{3.3}$$

The pitch motion remains a rotation around the spanwise axis of the foil and still described by equation 3.2. Although these kinematics produce an inherently three-dimensional flow, a roll-pitch flapping foil is more attractive when applied to an underwater vehicle. It allows more of the body to be rigid–like the shell of a turtle–and is therefore more practical for current actuation and payload technologies. In order to effectively parametrize the complex kinematics of roll-pitch flapping, they are conventionally expressed as equivalent heave-pitch kinematics at the 70% span of the foil, $r_{0.7}$, defined as:

$$r_{0.7} = r_0 + 0.7b, \tag{3.4}$$

where r_0 is the distance from the axis of rotation to the root of the foil and b is the span of the foil. This position is chosen because it divides the swept area of the foil in half. It is also consistent with conventional screw propeller notation, where the

pitch-to-diameter ratio is defined at 70% of the radius. The equivalent heave motion of the foil at this position is defined as:

$$h_{3D}(t) = r_{0.7}\phi_0 \sin(\omega t) = h_{0.7} \sin(\omega t) \tag{3.5}$$

3.1.1 Principal dimensionless parameters

A two-dimensional foil oscillating in heave and pitch and subject to a steady oncoming flow produces an elegant unsteady wake, called a reverse Kármán street [7]. This wake is the key to producing thrust with a flapping foil. It is composed of alternating sign vortices shed into the flow by the motion of the foil. Interactions between the vortices form an unsteady jet in the flow, which provides a time-harmonic thrust force. The properties of this wake are captured in three principal dimensionless parameters:

The width of the Kàrmàn street is determined primarily by the characteristic heave amplitude of its motion, h_c, and is captured by the heave-to-chord ratio. In heave-pitch flapping foils, this h_c is generally taken as the heave amplitude at the pitch axis of rotation, h_0, although some studies use the heave amplitude at the trailing edge of the foil, h_{TE}. In roll-pitch flapping foils, and the experiments presented in this study, h_c is taken as the heave amplitude at the pitch axis and the 70% span of the foil:

$$h_c = h_{0.7} = \phi_0(r_0 + 0.7b) \tag{3.6}$$

where r_0 is the radial distance from the roll axis of rotation to the root of the foil. Since the foils used in this study are not rectangular, the mean chord, $\bar{c}$ is used to nondimensionalize the heave amplitude:

$$\frac{h_c}{c} = \frac{h_{0.7}}{\bar{c}}. \tag{3.7}$$

The Strouhal number is a measure of the unsteady effects in the wake of an oscillating body; it is also the normalized heave velocity of the foil. It captures the downstream spacing of the vortices in the wake of the foil. For a roll-pitch flapping

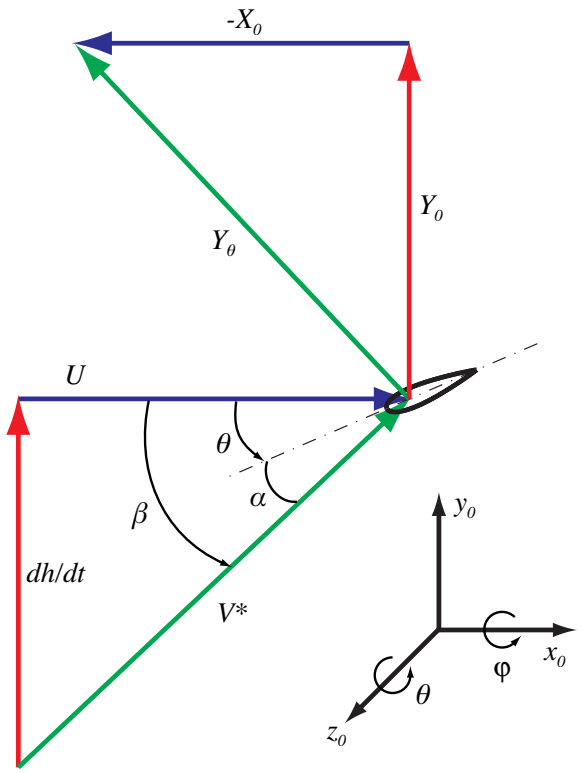

Figure 3-1
Vector diagram of velocities and forces in thrust producing solution of the attack angle.

foil, Strouhal number is defined:

$$S_t = \frac{h_c f}{U} = \frac{h_{0.7} f}{U}, \tag{3.8}$$

where $h_{0.7}$ is the heave amplitude defined in Equation 3.6, f is the flapping frequency in Hz, and U is the freestream velocity of the fluid.

The time-varying attack angle of the foil, $\alpha(t)$, governs the strength and number of vortices shed into the wake each flap cycle. It has two components. The first is the angle of the prescribed pitch motion, $\theta(t)$. The second is the angle induced by heave motion, $\beta(t) = \arctan\left(-\dot{h}(t)/U\right)$, which is defined with opposite sign to heave velocity so that it is consistent with the right-handed coordinate system. The equation for

attack angle can be reduced to a function of pitch amplitude and Strouhal number:

$$\alpha(t) = \beta(t) - \theta(t) = \arctan -(\dot{h}(t)/U) - \theta(t) \tag{3.9}$$

$$\alpha(t) = \arctan\left(\frac{-\omega h_{0.7}}{U}\cos(\omega t)\right) - \theta_0 \sin(\omega t - \psi) \tag{3.10}$$

$$\alpha(t) = -\arctan(\pi S_t \cos(\omega t)) + \theta_0 \cos(\omega t), \tag{3.11}$$

where $\psi = \pi/2$ has been used. Equation 3.11 has two solutions. One produces thrust (Figure 3-1) and the other produces drag. The maximum attack angle, α_{max}, is defined over one flap cycle.

$$\alpha_{max} = \max\left[\alpha(t)\right]_0^T \tag{3.12}$$

It is conventionally used as the third dimensionless parameter describing the flap kinematics and the wake they produce. Contours of constant α_{max} are plotted over a range of S_t and θ_0 on a bifurcation diagram in Figure 3-2.

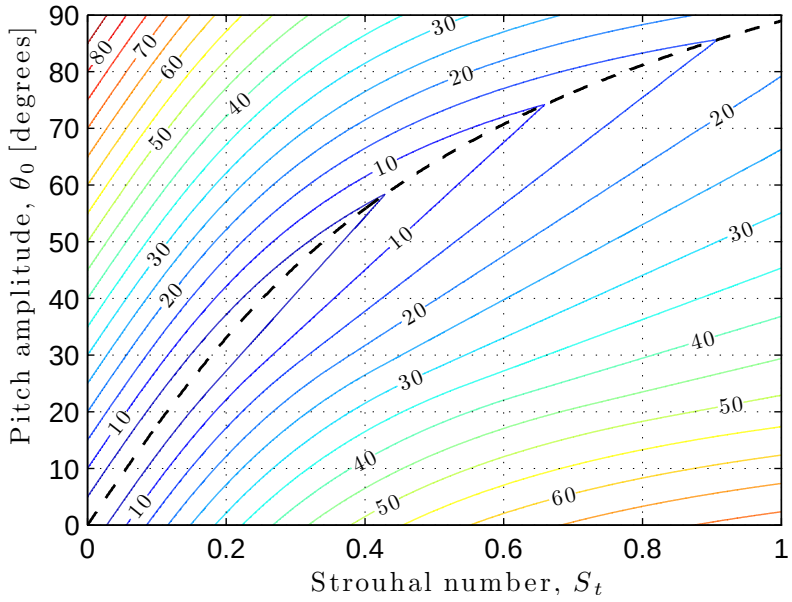

Figure 3-2
Bifurcation of α_{max}. Contours are maximum attack angle in degrees. The black dashed line is the boundary between thrust producing (lower right) and drag producing (upper left) solutions. Note that this figure applies to all flapping foils (heave-pitch or roll-pitch), provided that $\psi = \pi/2$.

Vortices are shed into the wake near extrema in the time rate of change of the attack angle, $\dot{\alpha}(t)$, or inflection points in the attack angle profile. This has been observed in previous experiments using two-dimensional kinematics [1, 10]. The strength of each vortex is proportional to the magnitude of $\dot{\alpha}(t)$ at the time it is shed. For a physical explanation, consider the simplified case of a two-dimensional rigid or semirigid foil:

$$\Gamma(t) = \frac{-Y_s}{\rho V} = -\frac{1}{2} V \bar{c} b C_{L_{2D}} \simeq -\pi V \bar{c} b \alpha(t), \tag{3.13}$$

where V is the apparent inflow to the foil, and $C_{L_{2D}} \simeq 2\pi\alpha$ is the lift coefficient of the foil. This relationship between the attack angle and the circulation shows why the vortices are shed at inflection points in the attack angle profile, and why their sign and strength depend on the magnitude of $\dot{\alpha}(t)$.

Since the attack angle is dependent on the arctangent of S_t (Equation 3.11), it is not a pure sinusoid. In fact, the arctangent term dominates at high S_t, degrading the attack angle profile and introducing additional inflection points, as shown in Figure 3-3.

When additional inflection points are introduced to the attack angle profile, additional vortices are shed into the wake. This has been observed in previous experiments [1, 10]. The new vortices are opposite sign to the originals (Figure 3-5); they degrade the clean reverse Kàrmàn street and add drag to the wake. The same thing happens when S_t is kept constant, but α_{max} is restricted to small values, as illustrated in Figure 3-4

Another consideration with roll-pitch flapping foils is that heave amplitude varies with span. This means that heave velocity, and therefore attack angle, also varies with span, as shown in Figure 3-6. This could potentially lead to different attack angle profile shapes over the span of the foil, but at the scales of these experiments, the effect is generally small.

The structure of the reverse Kàrmàn street can be controlled by choosing appropriate combinations of the three principal dimensionless parameters: $h_{0.7}/\bar{c}$, S_t, and α_{max}. Combinations of these parameters where high thrust and efficiency are

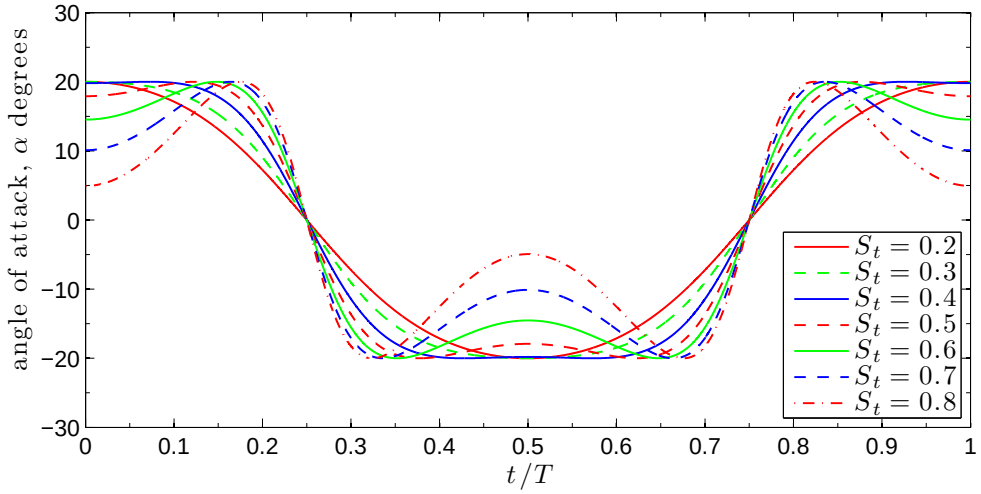

Figure 3-3
Degradation of α profile with increasing Strouhal number for $\alpha_{max} = 20°$. Note the introduction of new inflection points.

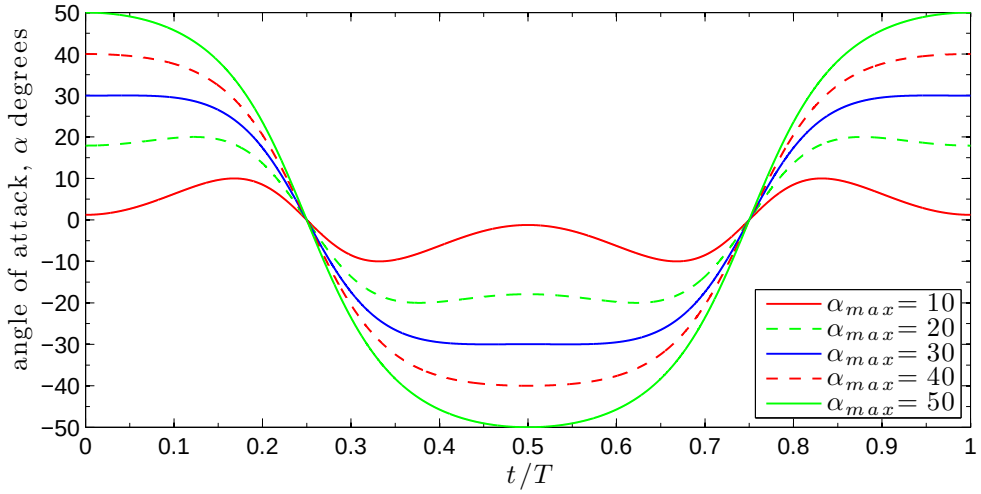

Figure 3-4
Degradation of α profile with decreasing maximum attack angle for $S_t = 0.5$. Note the introduction of new inflection points.

Figure 3-5
Schematic wake patterns showing showing a clean reverse Kàrmàn street (a) and one degraded by the introduction of parasitic drag vortices (b).

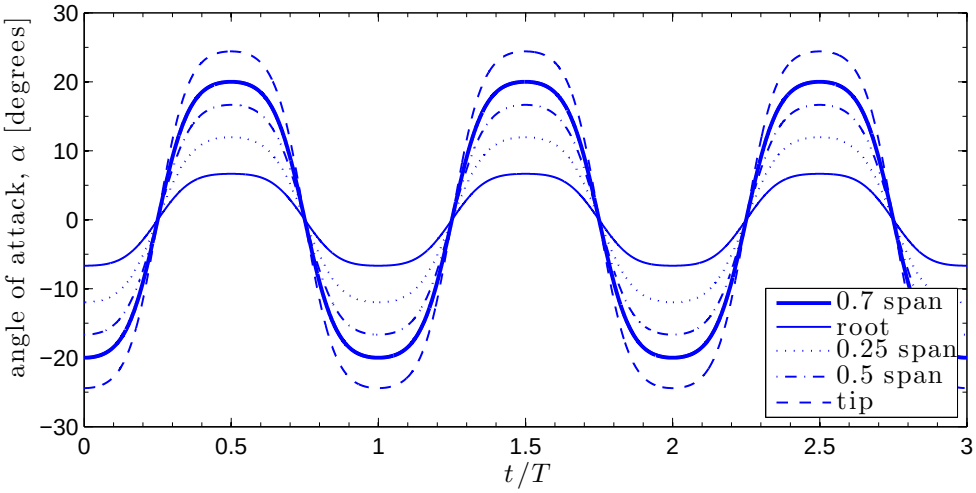

Figure 3-6
Variation of α profile over span of foil for flap kinematics: $h_{0.7}/\bar{c} = 1.5$, $S_t = 0.3$, $\alpha_{max} = 20°$

desirable operating points for a vehicle using flapping foil propulsion. Although the relationship between the wake structure and these parameters has been developed for two-dimensional kinematics, it also applies in principle to three-dimensional kinematics, where the two-dimensional vortices in the wake are replaced by three-dimensional vortex rings.

3.1.2 Performance metrics for a flapping foil

A flapping foil produces thrust or maneuvering forces to move a vehicle through a fluid. Just like the static control surface, performance metrics for a flapping foil are represented as parameters nondimensionalized by fluid and foil properties. Unlike a control surface, however, a flapping foil moves, and the work done it by the actuator is nondimensionalized by properties of the motion. The forces on a flapping foil are unsteady, but also cyclic, so averages are taken over one flapping period to determine the performance parameters.

Thrust is defined as the force in line with and opposing the fluid velocity. Using a right handed coordinate system with the x-axis aligned to the flow, as defined in

Figure 3-1, the average thrust is given as:

$$-\bar{X}_0 = -\frac{1}{T}\int_0^T X_0(t)dt. \tag{3.14}$$

Thrust is nondimensionalized in two different ways for a flapping foil. The first uses the planform area of the foil, $\bar{c}b$, and is useful for comparing the performance of foils with different geometries:

$$C_T = \frac{-\bar{X}_0}{\frac{1}{2}\rho U^2 \bar{c}b}. \tag{3.15}$$

The second thrust coefficient is nondimensionalized by the swept area of the foil, A_s:

$$C_{T_{SA}} = \frac{-\bar{X}_0}{\frac{1}{2}\rho U^2 A_s}, \tag{3.16}$$

where

$$A_s = 2\phi_0((r_0+b)^2 - r_0^2) \simeq 2h_{0.7}b. \tag{3.17}$$

This is more useful for comparing its performance to an ideal propulsor by actuator disk theory. The area used in this nondimensionalization is dependent on flap kinematics, and highlights one of the advantages of flapping foils: the effective area of the propulsor can be changed on the fly!

The average power consumed by the foil over one period of flapping is given as:

$$\bar{P} = \frac{1}{T}\int_0^T P(t)dt, \tag{3.18}$$

where $P(t)$ is the product of the torque and angular velocity in both motions, and will be defined explicitly in section 3.2.2. The average power is nondimensionalized as the power coefficient:

$$C_P = \frac{\bar{P}}{\frac{1}{2}\rho U^3 \bar{c}b}. \tag{3.19}$$

The hydrodynamic efficiency of the flapping foil is defined as the ratio of power output to power input:

$$\eta = \frac{P_{out}}{P_{in}} = \frac{C_T}{C_P}, \tag{3.20}$$

and measures how effectively a given foil shape with given flap kinematics can transfer power from the actuator to the fluid. It is useful to compare this measured efficiency to the ideal efficiency given by an actuator disk:

$$\eta_i = \frac{2}{1 + \sqrt{1 + C_{T_{SA}}}}, \tag{3.21}$$

which is an upper bound on the efficency for any physical propulsor producing thrust by imparting momentum to the fluid. Note that a lightly loaded propulsor is generally more efficient than a heavily loaded one, as shown by the inverse relationship between η and $C_{T_{SA}}$ in equation 3.21.

When a flapping foil is moving with symmetric kinematics, the net force will be thrust in the negative x-direction. This is because the lift forces on the foil are symmetric over one flap cycle. However, lift forces within each cycle are often much greater than the net thrust, so asymmetric flapping kinematics can produce large mean lift forces.

$$\bar{Y_0} = \frac{1}{T}\int_0^T Y_0(t)dt, \tag{3.22}$$

which is nondimensionalized as a mean lift coefficient:

$$C_L = \frac{\bar{Y_0}}{\frac{1}{2}\rho U^2 \bar{c} b}. \tag{3.23}$$

This can be used to generate maneuvering forces for a flapping foil vehicle. The lift production capabilities of the static foil can be compared to those of the dynamic foil, and the effects of different flapping kinematics can also be studied.

These performance metrics vary both with foil shape and with flapping parameters. This study will compare these quantities for the smooth control foil and the tubercled test foil over a wide range of parameters to determine the effect of tubercles on the performance of a flapping foil.

3.1.3 Previous Studies

Two dimensional flapping foil kinematics

Anderson, et. al. [1] measured power consumption and thrust production of harmonically oscillating foils at $R_e = 4 \times 10^4$. They measure a peak efficiency of $\eta = 0.87$. PIV visualization experiments at $R_e = 1 \times 10^3$ show that high efficiency conditions correspond to cases where a leading edge vortex interacts with trailing edge vorticity to produce a reverse Kàrmàn street. They identify the phase angle between heave and pitch motions, ψ, as the critical parameter in generating this wake. They study wake patterns for $h_0/c = 1.0$ at $0.1 < S_t < 0.6$ and $2^\circ < \alpha_{max} < 53^\circ$, producing a map in which they identify a region of 2S shedding, which produces a reverse Kàrmàn street, in $0.2 < S_t < 0.5$ and $7^\circ < \alpha_{max} < 50^\circ$. Experiments at higher S_t showed 2P shedding with two pairs of vortices, opposite in sign and different in magnitude, shed during each flap cycle. Other areas of the parametric space produced little or no thrust.

Read, et. al. [22, 23] measured the forces on a harmonically heaving and pitching foil to determine its thrust production and efficiency characteristics. These experiments were conducted in the MIT Tow Tank at $R_e = 4 \times 10^4$ for $h_0/c = \{0.75, 1.00\}$, and over a range of S_t, and α_{max}. They recorded efficiencies as high as $\eta = 0.715$ and planform area thrust coefficients as high as $C_T = 2.4$. While lower values were more typical, they noted a plateau of high efficiency ($\eta > 0.5$) that also included high thrust cases. They also investigated the effect of the phase angle between heave and pitch motion, concluding that $\psi = 90^\circ - 100^\circ$ was best-suited to thrust production. They added a static pitch bias angle, θ_{bias}, to the foil motion to produce a net lift force in addition to thrust, with application to generating maneuvering forces.

Beal, et. al. [3, 13, 2] studied wake synchronization in flapping foil propulsion. They observed live and euthanized rainbow trout (*Oncorhynchus mykiss*) in the Kármán street drag wake behind a cylinder in a flow. They noted that the live fish would position itself four cylinder diameters downstream from the cylinder and tune its motion with the vortices shed by the cylinder in what they termed the Kármán

gait. The dead fish passively synchronized its motion and was propelled upstream by its interaction with the vortices in the cylinder wake. This suggested the possibility of a flapping foil simultaneously extracting energy and producing thrust in the wake behind a cylinder. A passively mounted high aspect ratio foil was placed in the wake of a cylinder to confirm this. Heave and pitch motions were observed with a phase angle of $\psi = 90°$. Although the magnitudes of the measured thrust and power coefficients, $C_T = 0.017$ and $C_P = -0.0071$ were small, they were an order of magnitude larger than measurement uncertainty levels, confirming simultaneous thrust production and power extraction. This has yet to be applied in a man-made vehicle, and that is likely to be a very complex undertaking, but it is one of the interesting areas where flapping foils show great promise.

Read, et. al. [23] noted the importance of the attack angle profile in time. By introducing higher order harmonics into the heave motion, they simultaneously increased thrust coefficient and efficiency. Hover, et. al. [10] extend that work by explicitly defining the attack angle profile and solving the inverse problem for the heave motion profile. Mapping the attack angle profile to a cosine significantly improved thrust production and efficiency in high S_t test cases where simple harmonic flapping suffers from degradation of the attack angle profile, as discussed in section 3.1.1. Prempraneerach, et. al.[21] increased the propulsive efficiency of a heave-pitch flapping foil by introducing chordwise flexibility. Flexible foils consistently outperformed the rigid control group in $0.15 < S_t < 0.45$, increasing efficiency with little loss–sometimes substantial increase–in thrust. They observed this effect both in simple harmonic flapping and using higher order heave harmonics as in [23]. Foils with shore A60 flexibility provided the most improvement, providing similar thrust-efficiency performance to a conventional Kirsten-Boeing screw-type propeller.

Three dimensional flapping foil kinematics

Flores [6] conducted experiments on a rigid flapping foil using roll-pitch kinematics in the water tunnel in the MIT Marine Hydrodynamics Laboratory. Her foil had a NACA 0015 cross section with a tapered planform and $\mathcal{R} = 4.5$. She investigated the thrust

production capability of simple harmonic flapping for $h_{0.7}/\bar{c} = \{1.0, 1.5\}$, $0.2 < S_t < 0.8$ and $15° < \alpha_{max} < 50°$. The maximum planform area thrust coefficient $C_T = 2.07$ was recorded at $h_{0.7}/\bar{c} = 1.5$, $S_t = 0.8$ and $\alpha_{max} = 40°$. She performed maneuvering experiments with nonzero pitch bias, θ_{bias}, achieving mean lift coefficients near $C_L = 4$. She also measured the forces produced by an impulsively started foil. Using phase-averaged LDV data she observed a thrust jet in the wake of about $1.5 \times U$ at $r_{0.7}$. This data also validated the approximation of the wake width as $2h_{0.7}$.

Polidoro [20] designed an improved roll-pitch actuator for use on a flapping foil autonomous underwater vehicle (AUV). He conducted tests using rectangular NACA 0012 foils of $\mathcal{AR} = \{3, 4, 5, 6\}$ over a wide range of flap parameters. The maximum planform area thrust coefficient $C_T = 7.2$ was recorded at $h_{0.7}/\bar{c} = 3.2$, $S_t = 1.2$ and $\alpha_{max} = 40°$ with the foil of $\mathcal{AR} = 4$.

Mcletchie [16] uses a small six-axis submersible dynamometer mounted between the actuator and the foil to simultaneously measure power consumption and thrust production. His foil was rigid with a NACA 0012 cross-section, a tapered planform, and $\mathcal{AR} = 4.5$. This provides efficiency measurements independent of actuator characteristics. His thrust measurements compare well to previous results by Flores [6] and Polidoro [20]. Efficiency measurements in highly loaded cases appeared reliable when compared to efficiencies previously measured in two-dimensional flapping. However, the small magnitude of the forces measured, coupled with unmeasured backlash in the motion profiles, led to unrealistic results in lightly loaded, high efficiency cases.

Lim [15] attached potentiometers directly to the output shafts of the actuator, providing a direct measurement of roll and pitch angles. He conducted experiments at $h_{0.7}/\bar{c} = \{1.0, 1.5, 2.0\}$, $0.2 < S_t < 0.6$ and $15° < \alpha_{max} < 45°$ using the same foil as Mcletchie in [16]. His maximum thrust coefficient $C_T = 2.09$ was measured at $h_{0.7}/\bar{c} = 1.5$, $S_t = 0.6$ and $\alpha_{max} = 30°$. His maximum efficiency $\eta = 0.828$ was measured at $h_{0.7}/\bar{c} = 1.5$, $S_t = 0.3$ and $\alpha_{max} = 20°$. Although he performed repeated tests of these parameters, this efficiency may still be artificially high because of small forces measured and other experimental concerns (see Appendix A.3.1). He studied the vortex wake on planes at the 50% and 80% span of the foil (defined at zero roll)

for four sets of flap parameters. Two predominant patterns were observed: a 2S pattern corresponding to the reverse Kàrmàn street, and a 2P pattern similar to the one observed by Anderson in [1].

3.2 Experimental Setup and Procedures

3.2.1 Second-generation flapping foil actuator

The flapping foil actuator used in these experiments is a modified version of the actuator used on the Biomimetic Flapping Foil AUV at the MIT Towing Tank. Two cylindrical watertight housings are supported by an aluminum frame. The large stationary housing contains a DC servomotor (Moog Components Group, Type C13G) that drives roll motion. The smaller housing moves in roll and contains another DC servomotor (Moog Components Group, Type C23G), oriented 90 °to the roll axis, that drives pitch motion. Encoder signal conditioners, discussed in Appendix A.3.2, are installed on each axis to mitigate electromagnetic interference noise on the encoder outputs. This was necessary to prevent corrupted encoder counts in the control loop. Hollow-shaft potentiometers (Inscale Technology, GL200) are attached directly to the roll and pitch output shafts. These measure the angular position including the backlash that is present on both roll and pitch axes. Potentiometer calibration techniques and results are discussed in Appendix A.1.2. The whole module is mounted through the top window of the water tunnel, as shown in Figure 3-7. A free-flooded offset box positions the setup with the foil in the center of the test section, and a thermoformed ABS fairing isolates the actuator, sensor, and wiring from the freestream flow.

A two axis motion controller (National Instruments, PXI-7352) generates command signals for the actuator. The command signals are converted to 50 kHz PWM inputs to each motor by an integrated servo drive with power supply (National Instruments, MID-7652). The system uses a closed-loop PID controller.

Motion profiles are defined by entering roll and pitch amplitudes and the flapping frequency into a LabVIEW virtual instrument interface. The foil starts in the home

Figure 3-7
Flapping foil actuator installed in the top window of the water tunnel. The tubercled test foil is mounted in this picture, and the AMTI dynamometer is visible mounted between the foil and the actuator.

position at $\phi = 0$, $\theta = 0$. Five seconds of null offset data are recorded at the beginning of each test before motion starts. The foil then ramps up to full amplitude motion over the course of two flap periods, to avoid damaging the actuator with high accelerations or overheating the motors with high starting currents. Data is then recorded for at least twenty full flap cycles, after which the foil ramps back down and five more seconds of null offset data are recorded at the end of the test.

3.2.2 Force measurement, acquisition, and processing

The same six-axis submersible dynamometer is used as in the static study (Section 2.2). Sensor calibration and alignment are discussed in Appendix A. The data acquisition setup is also the same as the static experiments, with all channels recorded simultaneously at 500 Hz by a 16-bit analog-to digital converter (National Instruments, PXI-6031E) through various signal connection and amplification modules.

Raw voltages with the null offset removed are shown for overlapping three-flap bins in Figure 3-8. This data is postprocessed using a third order Butterworth low-pass filter with a cutoff frequency of 10 Hz for the force data and 20 Hz for the angular position data.

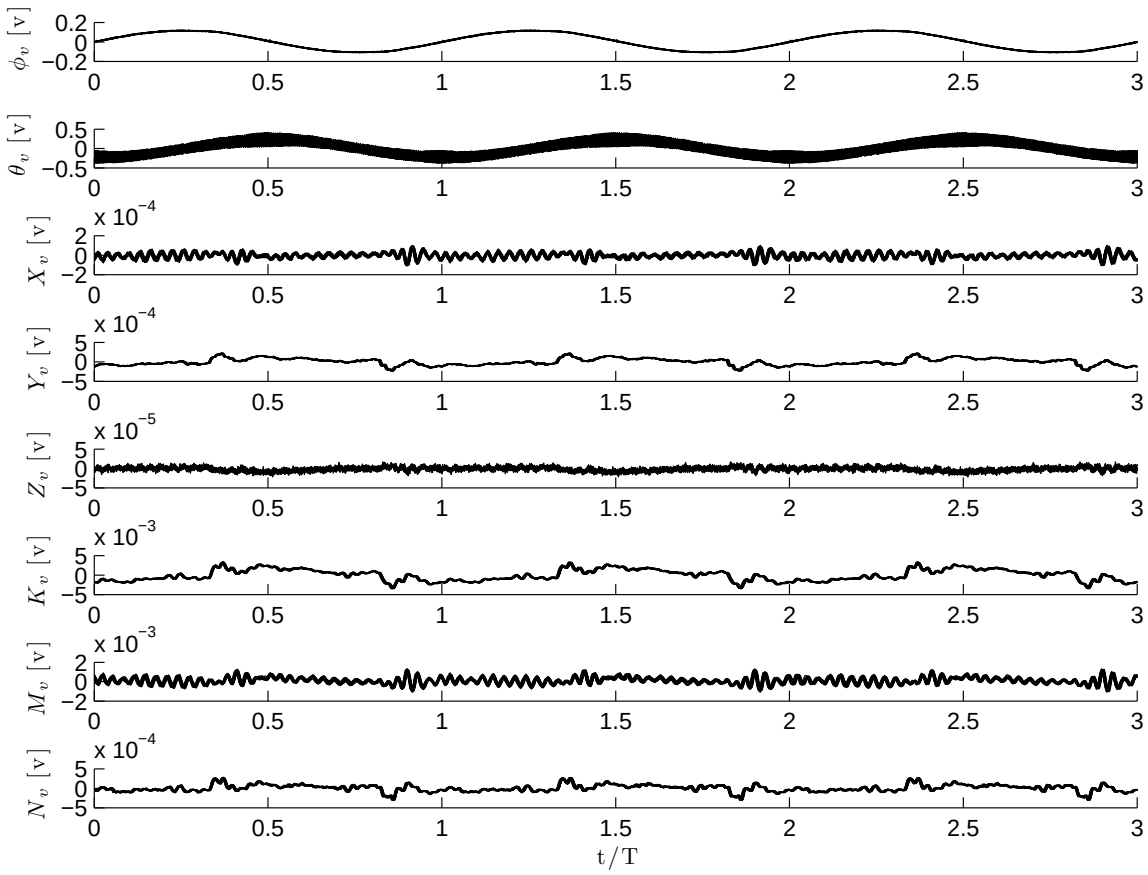

Figure 3-8
Raw data split into overlapping three flap bins, all plotted on top of each other.
Dimensionless parameters for this test are: $S_t = 0.3$, $h_{0.7}/\bar{c} = 1.5$, $\alpha_{max} = 20°$.

Angular positions are then compared to a sine of the commanded frequency to check that motion profile is correct. Figure 3-9 shows the measured angular position, the first order fit, and the residuals. Some backlash is evident at the extrema.

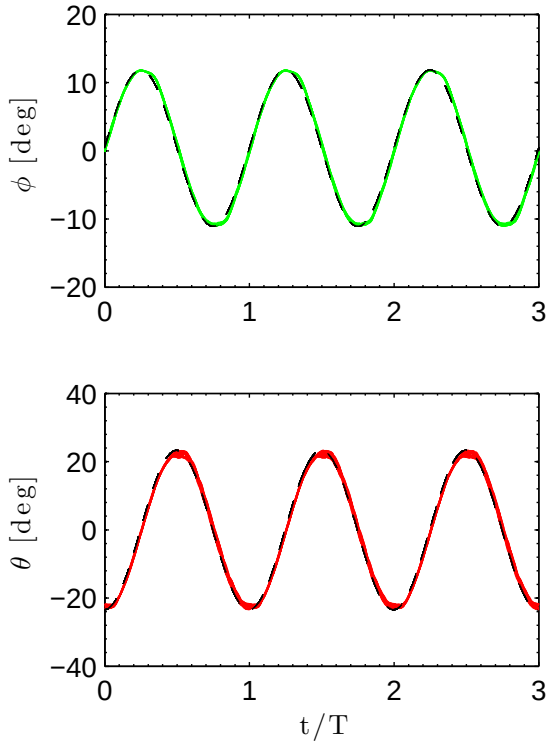

Figure 3-9
Angular positions recorded by the potentiometers, including first order sinusoid fits.

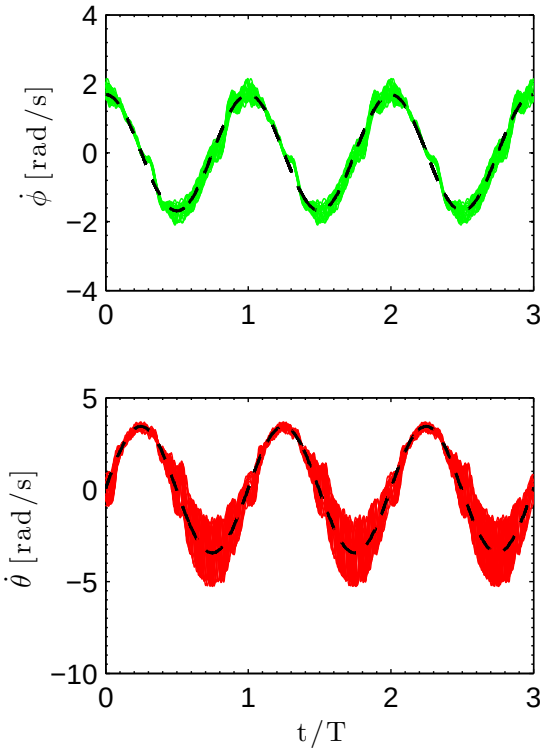

Figure 3-10
Angular velocities as the time derivative of angular position fits (dashed lines) and as the discrete approximation.

Angular velocities are taken as the time derivative of the sine fitted to the angular position. This method was chosen because it provides a more accurate physical representation of the motion than using a discrete approximation of the time derivative, as shown in Figure 3-10. It is also important for the uncertainty analysis applied to the data, as using the discrete approximation would cause the uncertainty to grow with sampling frequency.

Raw voltage outputs from the AMTI sensor are converted to forces according to Equation 3.24,

$$\boldsymbol{X}_s = \bar{\boldsymbol{S}}^{-1}\boldsymbol{V}, \tag{3.24}$$

where the sensitivity matrix $\bar{\boldsymbol{S}}$ is the same used previously in the static experiments, and is given in Appendix A.1.1. These sensor-referenced forces are then rotated by the foil misalignment angle, ϵ, into the foil-reference frame. This is also the pitch-reference frame, as it moves with the pitch angle.

$$\begin{Bmatrix} X_\theta \\ Y_\theta \\ Z_\theta \\ K_\theta \\ M_\theta \\ N_\theta \end{Bmatrix} = \begin{bmatrix} \cos\epsilon & -\sin\epsilon & 0 & 0 & 0 & 0 \\ \sin\epsilon & \cos\epsilon & 0 & 0 & 0 & 0 \\ 0 & 0 & 1 & 0 & 0 & 0 \\ 0 & 0 & 0 & \cos\epsilon & -\sin\epsilon & 0 \\ 0 & 0 & 0 & \sin\epsilon & \cos\epsilon & 0 \\ 0 & 0 & 0 & 0 & 0 & 1 \end{bmatrix} \begin{Bmatrix} X_s \\ Y_s \\ Z_s \\ K_s \\ M_s \\ N_s \end{Bmatrix} \tag{3.25}$$

Pitch moment, $N_\theta(t)$, is taken here because it is the actual pitch moment from the actuator to the foil.

These forces are then rotated by pitch angle, $\theta(t)$, into the roll-reference frame. This is written more compactly as:

$$\boldsymbol{X}_\phi = \boldsymbol{J}_\theta \boldsymbol{X}_\theta, \tag{3.26}$$

$$\text{where } \boldsymbol{J}_\theta = \begin{bmatrix} \boldsymbol{R}_\theta & \boldsymbol{0}_{3\times3} \\ \boldsymbol{0}_{3\times3} & \boldsymbol{R}_\theta \end{bmatrix} \text{ and } \boldsymbol{R}_\theta = \begin{bmatrix} \cos\theta & -\sin\theta & 0 \\ \sin\theta & \cos\theta & 0 \\ 0 & 0 & 1 \end{bmatrix} \tag{3.27}$$

Roll moment, $K_\phi(t)$, and roll side force, $Y_\phi(t)$, are taken here to compute the roll moment from the actuator to the foil.

Roll-referenced forces are rotated by $\phi(t)$ into the lab reference frame.

$$\boldsymbol{X}_0 = \boldsymbol{J}_\phi \boldsymbol{X}_\phi, \tag{3.28}$$

$$\text{where } \boldsymbol{J}_\phi = \begin{bmatrix} \boldsymbol{R}_\phi & \boldsymbol{0}_{3\times3} \\ \boldsymbol{0}_{3\times3} & \boldsymbol{R}_\phi \end{bmatrix} \text{ and } \boldsymbol{R}_\phi = \begin{bmatrix} 1 & 0 & 0 \\ 0 & \cos\phi & -\sin\phi \\ 0 & \sin\phi & \cos\phi \end{bmatrix} \tag{3.29}$$

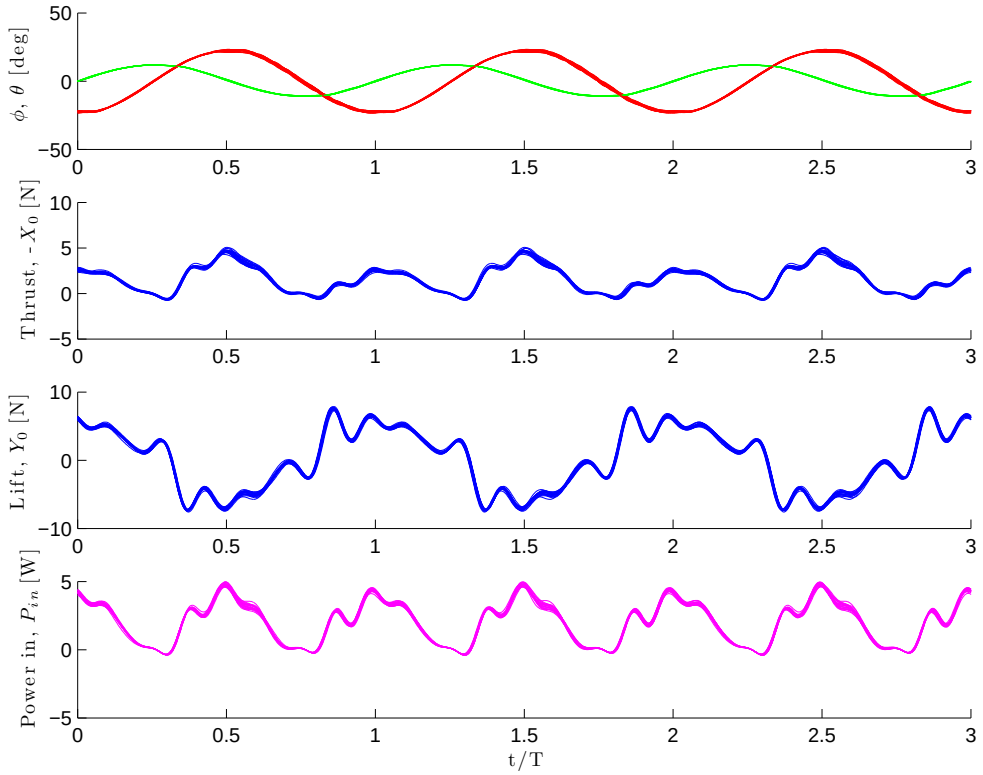

Figure 3-11
Resultant lab-referenced thrust, $-X_0$, lift, Y_0, and input power, P_{in} as time traces separated into overlapping three-flap bins. Dimensionless parameters for this test are: $S_t = 0.3$, $h_{0.7}/\bar{c} = 1.5$, $\alpha_{max} = 20°$.

The input power is now calculated from the angular velocities and intermediary moments in pitch and roll:

$$P(t) = -(K_\phi(t) + r_s Y_\phi(t))\dot{\phi}(t) - N_\theta(t)\dot{\theta}(t), \tag{3.30}$$

where the $r_s Y_\phi(t)$ term accounts for the fact that the sensor axis is radially translated from the actuator roll axis.

The lab referenced forces and input power are shown in Figure 3-11. These are analogous to the forces on a vehicle moving through the water, and the power required from that vehicle to generate these forces. The lift force is symmetric and periodic with the same dominant frequency as the flapping motion. The thrust force and input power, which correlate very well in time, have a dominant frequency twice that of the flapping motion. Some small asymmetry in the results of this test is evident, as the

thrust peaks are not all the same height.

Time averages are taken over each flap period to compute mean force and power coefficients. These coefficients are plotted as contours over the parametric space in Figures 3-13 and 3-14.

3.2.3 Reynolds number effects

For a given S_t, there are a range of possible flow velocities and flapping frequencies. The actuator provides reliable motion profiles up to a flapping frequency of about 1.5 Hz. Experiments are conducted at the highest tunnel speed, and therefore the highest R_e and f possible, in order to measure greater magnitude forces. This is expected to minimize error in the measurements due to operating low in the range of the force sensor, but a small set of tests was conducted to provide confirmation.

Figure 3-12 shows measured thrust coefficient and efficiency for both foil types over a range of R_e. Four sets of flapping parameters were investigated for each foil. Type I and II flapping characterizes high efficiency conditions. It is described by the parameters: $S_t = 0.3$, $h_{0.7}/\bar{c} = \{1.5, 2\}$, $\alpha_{max} = 20°$. Type III and IV flapping characterizes high thrust conditions. It is described by the parameters: $S_t = 0.6$, $h_{0.7}/\bar{c} = \{1.5, 2\}$, $\alpha_{max} = 30°$. Three separate tests were run for each foil and set of flap kinematics at seven different Reynolds numbers, $1 \times 10^4 < R_e < 4 \times 10^4$. The measured thrust coefficient shows little dependence on Reynolds number for either foil, but results tend to converge slightly better as R_e increases. Efficiency in type I and II flapping has a broad spread for low R_e. The results collapse with increasing R_e. This is also true with type III and IV flapping, although the initial spread at low R_e is not nearly as pronounced. These results indicate that the highest combination of flow speed and flapping frequency should be used, as a rule, to obtain consistent measurements.

Results presented in Figure 3-12 are also tabulated in Appendix B.

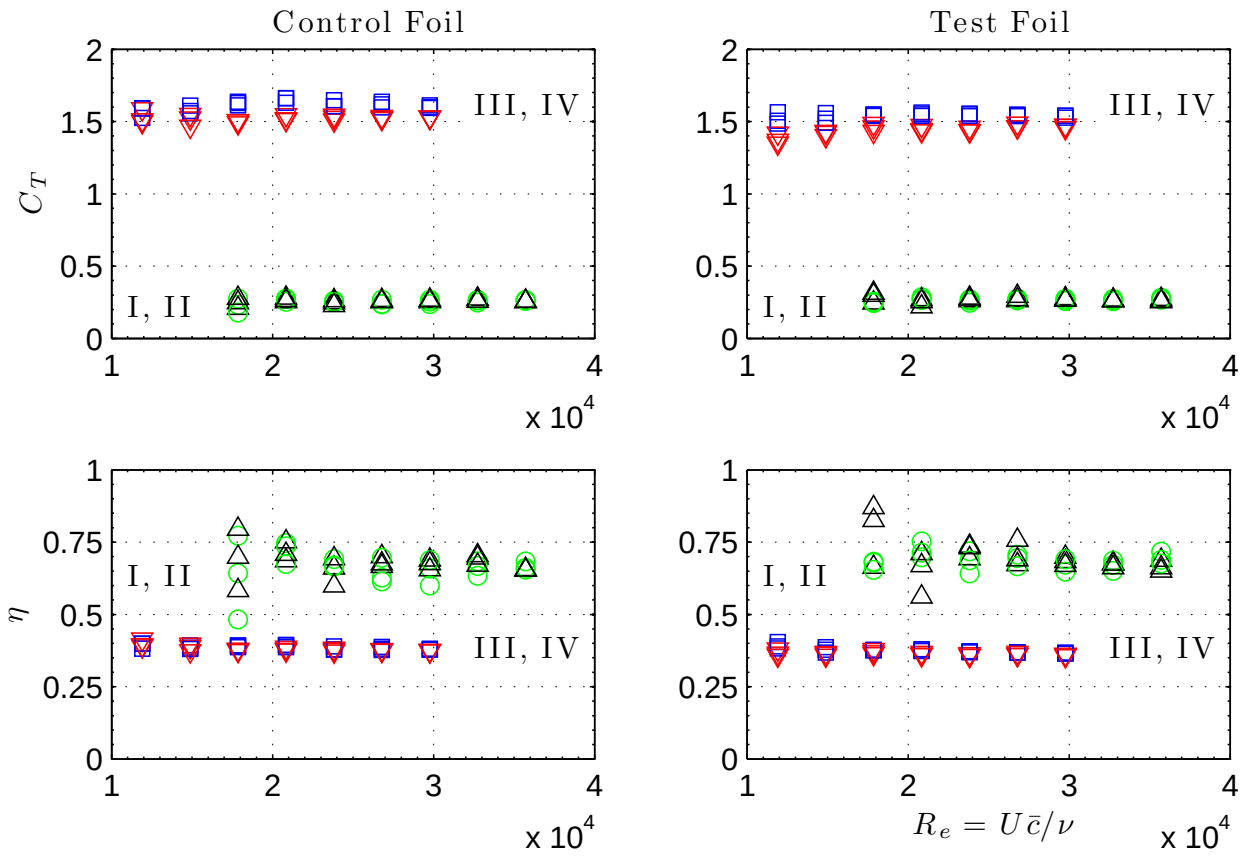

Figure 3-12
Repeated Reynolds number tests. Note the spread in measured performance, especially efficiency, in low R_e tests. Type I (○) and II (△) are high efficiency parameter sets; type III (□) and IV (▽) are high thrust.

3.3 Thrust production experiments

3.3.1 Control foil

The thrust production and hydrodynamic efficiency are the primary quantities of interest for a flapping foil vehicle in cruising mode. Figure 3-13 presents the planform area thrust coefficient and the hydrodynamic efficiency of the smooth control foil as contours plotted over the parametric space. Strouhal number was varied from 0.2 to 0.8, maximum attack angle from 10°to 60°, and heave amplitudes of 1.0, 1.5, and 2.0 were investigated. Dots on these contours mark the combinations of parameters used in each experiment. Exact quantities for each experiment are tabulated in Appendix B.

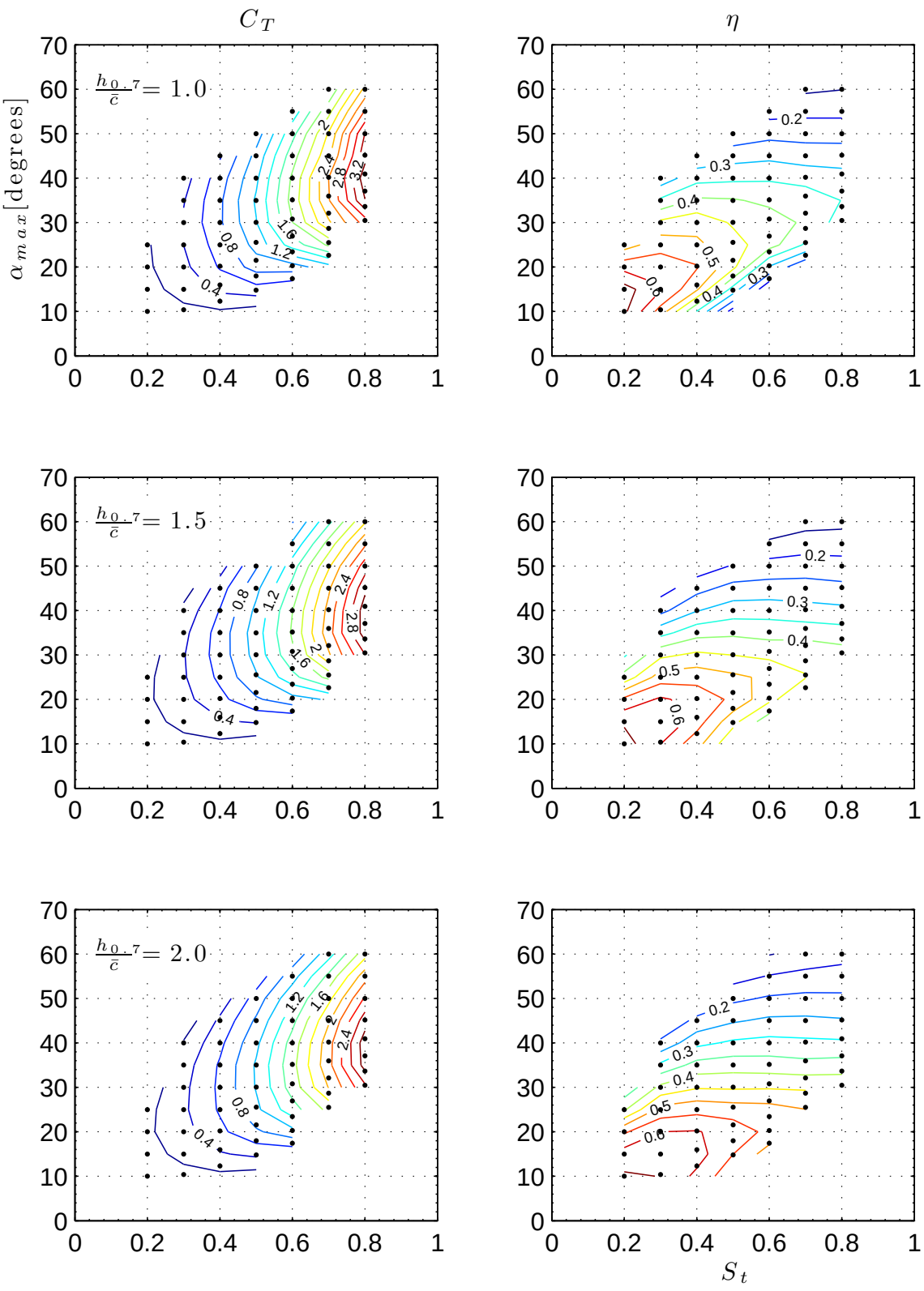

Figure 3-13
Contour plots of thrust coefficient and hydrodynamic efficiency using the smooth control foil.

The upper left limit of the experiments is near the line of zero pitch motion. Beyond that the pitch amplitude required for a given attack angle becomes negative and the foil would basically be flapping backwards, resulting a drag wake. The lower right limit of the experiments approaches the terminal S_t. Beyond that is another region where flapping parameters transition from thrust-producing to drag-producing, as shown in the bifurcation of the maximum attack angle in Figure 3-2. This also coincides with large pitch amplitudes which would cause the actuator to stall out in some high flap frequency cases. As a rule, pitch amplitude was kept below 45°.

Performance tends to decline slightly as heave amplitude is increased, but trends across S_t and α_{max} are the same for each heave amplitude. The case for $h_{0.7}/\bar{c} = 1.0$ is discussed in depth:

Thrust increases strongly with S_t. It also increases more gently with α_{max} until it reaches a maximum in the region $25° < \alpha_{max} < 45°$. The maximum thrust coefficient measured using the smooth control foil was $C_T = 3.51$ at $S_t = 0.8$, $\alpha_{max} = 40.9°$, and $h_{0.7}/\bar{c} = 1.0$. A line of maximum thrust across the parametric space would show where a flapping foil vehicle should operate in conditions requiring maximum acceleration and maneuvering authority, such as a turbulent surf zone.

High efficiency is found at low S_t and α_{max}, which is expected both due to the light thrust loading in that region. The maximum efficiency of $\eta = 0.678$ was recorded at $S_t = 0.2$, $\alpha_{max} = 15°$, and $h_{0.7}/\bar{c} = 1.0$. Most efficient operation for a given S_t is approximately linear, extending from $\alpha_{max} \simeq 15°$ at $S_t = 0.2$ to $\alpha_{max} \simeq 35°$ at $S_t = 0.8$. A vehicle should operate somewhere along this line during cruising. Above and to the left of this line efficiency decreases gently with α_{max}, but it drops steeply below and to the right of it. Power input is increasing in this region, but thrust remains constant or begins to decrease. This is the region where additional inflection points appear in the attack angle profile. Power is being diverted into the growing parasitic drag vortices that are degrading the reverse Kàrmàn street.

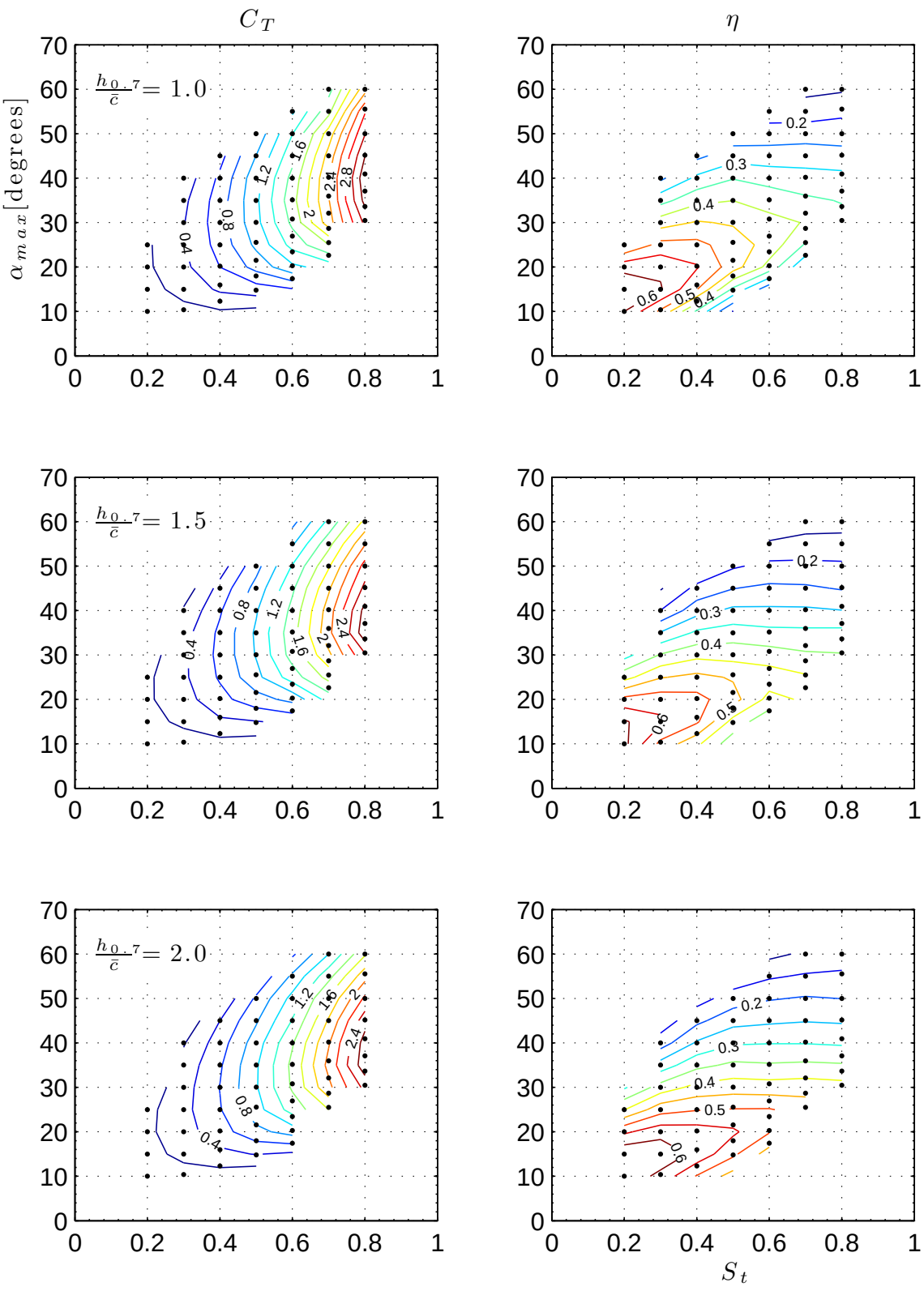

Figure 3-14
Contour plots of thrust coefficient and hydrodynamic efficiency using the tubercled test foil.

3.3.2 Test foil

The thrust coefficient and hydrodynamic efficiency of the tubercled test foil, given in Figure 3-14, show the same trends identified and discussed in the results of the control foil. However, the actual magnitudes of thrust and efficiency are generally lower across the whole parametric space. The maximum thrust coefficient measured using the test foil was $C_T = 3.37$ at $S_t = 0.8$, $\alpha_{max} = 37.1°$, and $h_{0.7}/\bar{c} = 1.0$ A maximum efficiency of $\eta = 0.663$ was recorded at $S_t = 0.2$, $\alpha_{max} = 10$, and $h_{0.7}/\bar{c} = 1.5$.

Thrust output and power input for both foils are compared directly in Figure 3-15 for $h_{0.7}/\bar{c} = 2.0$. The test foil produces 6.22% less thrust than the control foil on average over the range of S_t and α_{max} tested. In lightly loaded conditions at low S_t and α_{max}, the thrust production of the two foils is similar. The test foil produces 4.76% more thrust than the control foil at $S_t = 0.2$ and $\alpha_{max} = 15°$, but this is in a low thrust area, so it only translates to a C_T increase of 0.0065. The test foil performs worse as loading increases. The largest percentage difference in C_T is -17.59% at $S_t = 0.4$ and $\alpha_{max} = 12.3°$, and the largest magnitude difference in C_T is -0.25 at $S_t = 0.8$ and $\alpha_{max} = 40.9°$.

The power consumed by the foils is virtually the same, on the other hand. On average, the test foil consumes just 0.61% less power than the control foil over the parametric space. The largest percent difference cases are where it consumes 7.09% more at $S_t = 0.2$ and $\alpha_{max} = 10°$, and 5.89% less power at $S_t = 0.4$ and $\alpha_{max} = 12.3°$.

Since the test foil produces less thrust with the same power consumption, it is less efficient in flapping than the control foil. This result is a bit anticlimactic, but it is still important to try to understand what causes it.

The test foil is absorbing the same amount of energy as the control foil. So where is that energy going if it isn't contributing to the thrust? One possible explanation is that it is going into vortical structures other than the reverse Kàrmàn street. Recall that is what happens when the foil flaps below the line of maximum efficiency–energy is diverted to generate parasitic drag vortices produced by the corrupt attack angle profile. Also recall the chordwise vortical structures generated by the tubercles in

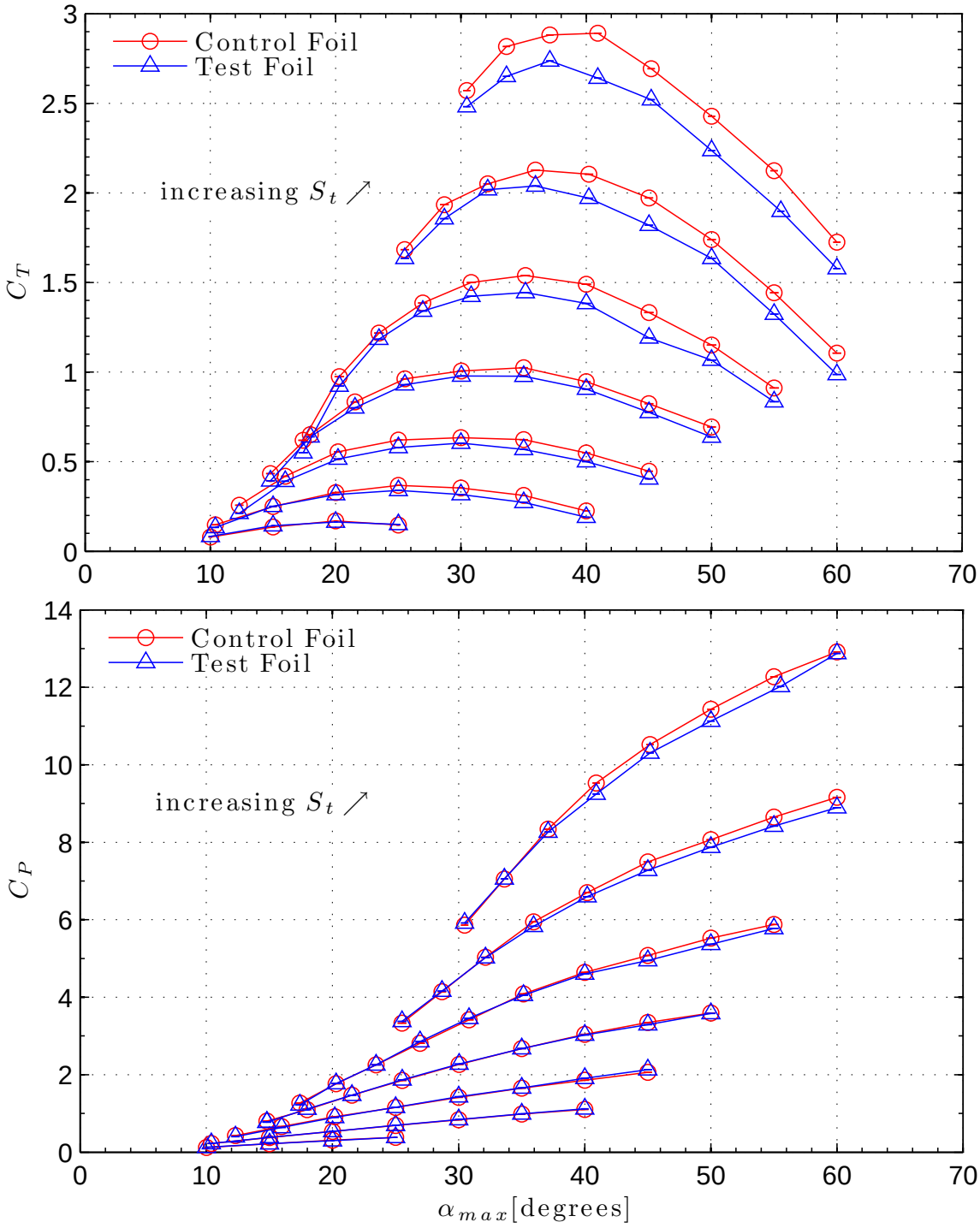

Figure 3-15
Thrust production power consumption using both foils with $h_{0.7}/\bar{c} = 1.0$.

the static foil study. These do not contribute to the thrust jet in the reverse Kàrmàn street. Actually, these structures are orthogonal to the vortices generated by flapping, which are predominantly spanwise-oriented. It is likely that the interaction between these two types of vortical structures breaks down the thrust wake, with the same end result as the introduction of drag vortices caused by the corrupt attack angle profile. This would explain the loss of thrust with little change in power. The difference here is that the vortical structures generated by the tubercles are not restricted to one area of the parametric space. In fact, these structures seem to grow in strength and absorb more energy as loading increases.

3.3.3 Discussion

The trends observed in these results are consistent with those reported previously for roll-pitch flapping foils [15, 16, 14, 6, 20]. The parametric space of these results is more extensive than explored in [15, 16, 6]. The magnitude of both C_T and η is somewhat lower than measured by Lim [15]. Although the foil used in this study has a thicker cross-section and a different planform shape, measurements made using the same foil that Lim used also yielded lower magnitude results. This discrepancy is most likely due to issues related to the ground loop he experienced. This is discussed further in Appendix A.3.1.

The control foil performs better than the test foil, but how well do either of them stand up to the ideal propulsor? Figure 3-16 plots the efficiency of both foils as a function of the swept area thrust coefficient, $C_{T_{SA}}$. Their performance is compared to the theoretical actuator disk, which represents an upper bound on the thrust-efficiency performance of any real propulsor. In very lightly loaded cases, the flapping foil performs as high as 60% to 70% of the ideal efficiency. As loading increases, the most efficient combinations of flap parameters only reach 40% to 50% of the ideal efficiency.

This thrust-efficiency performance is below what can be expected for a conventional screw-type marine propeller, which is somewhat disappointing. However, the technology and understanding of flapping foil propulsion are much younger than for

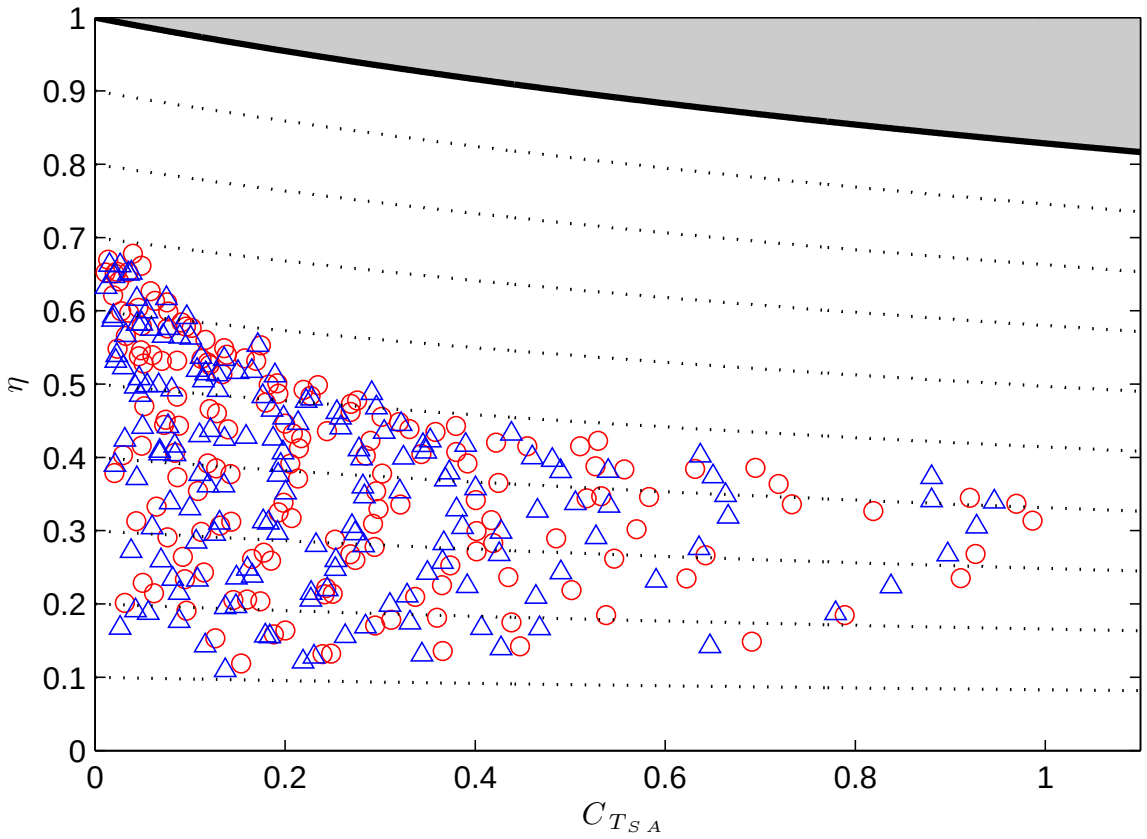

Figure 3-16
Swept area thrust coefficient versus hydrodynamic efficiency for smooth control foil (○) and tubercled test foil (△). The thick line at the top of the plot denotes the maximum efficiency possible with an ideal thruster (actuator disk). Dotted lines below indicate 90% to 10% of ideal efficiency.

screw propellers. Researchers have already improved thrust and efficiency of heave-pitch flapping foils by making them flexible or by explicitly specifying attack angle profiles [10, 21]. It is also important to remember that flapping foils produce forces very quickly, and the primary goal in using them is to achieve increased maneuverability, increasing the range of conditions that marine vehicles are capable of operating in.

3.4 Maneuvering force experiments

Maneuverability ultimately comes down to a question of how much thrust and lift a vehicle can generate, and how quickly. The most straightforward way to produce these

maneuvering forces with a flapping foil this is to add a nonzero static bias angle to one of the motions. A roll bias, ϕ_{bias}, changes the line of action along the longitudinal axis of the actuator. This is important for a vehicle, especially with multiple foils, but is not discussed in this study because of the limited space for roll motion within the water tunnel. Furthermore, since the tunnel setup constrains the actuator to be aligned aligned with the flow, the results would not add to understanding beyond those of basic thrust production.

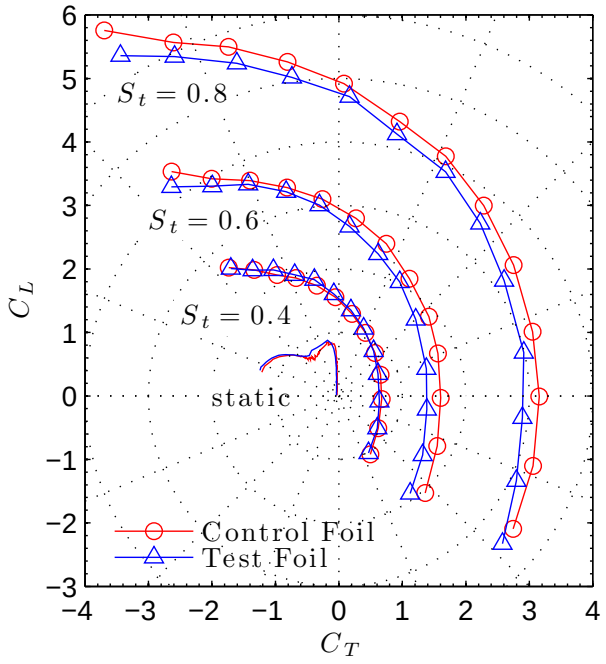

Figure 3-17
C_T vs. C_L polar diagram for maneuvering force tests. $\alpha_{max} = 40°$, and $h_{0.7}/\bar{c} = 1.5$.

A pitch bias, θ_{bias}, on the other hand, produces a net lift force perpendicular to the flow. Experiments were conducted using both control and test foils at three strouhal numbers, $S_t = \{0.4, 0.6, 0.8\}$, over a range of pitch bias angles, $-10° < \theta_{bias} < 50°$. Maximum attack angle was kept constant at $\alpha_{max} = 40.0°$. All three heave amplitudes were tested, but the difference in performance was small. Results for $h_{0.7}/\bar{c} = 1.5$ are discussed here.

Figure 3-17 shows the direction of net force as a polar diagram between mean C_T and C_L. Discrete data points are tests at different θ_{bias}. Tests which fall on the right side of the polar, in positive C_T, are combinations of parameters that would accelerate

a vehicle through a turn; tests on the left side would slow it down. Similarly, tests with positive or negative C_L would turn the vehicle right or left.

It is readily apparent that the maneuvering forces produced by the flapping foil are much greater than a conventional static control surface is capable of producing. The magnitude of the maneuvering force increases with S_t, which is consistent with the thrust production experiments discussed in the previous sections. This is also consistent with observations in previous studies using different foils [14, 6, 23]. The performance of the test foil and the control foil is similar for the lightest loading at $S_t = 0.4$, but the test foil does worse than the control as loading is increased, just like in the thrust production experiments.

3.5 Conclusions

This study has investigated the effect of leading edge tubercles on the performance of a flapping foil. It began by introducing the kinematics of two- and three-dimensional flapping foils. The principal dimensionless parameters of flapping foil propulsion were then introduced and physically related to the reverse Kármán street wake. Important considerations regarding the attack angle profile were discussed. Performance metrics were defined and identified as the primary objective of the experiments, and a selection of previous experimental work on flapping foils was summarized.

Specifics of this study began with the introduction of the flapping foil actuator, after which the methods of force measurement and data processing were outlined. Experiments generating thrust and maneuvering forces were conducted over a wide parametric space. Common trends–consistent with previous studies–were observed in the results, and physical reasons for these trends were given.

The tubercled test foil produced less thrust while consuming the same amount of power, and was therefore less efficient than the smooth control foil. The difference in performance was greater for parameters where the flapping foil was heavily loaded. Results from the maneuvering tests were consistent with the thrust production tests.

A likely explanation for this degraded performance was suggested: that the vor-

tical structures generated by the tubercles and observed in the static study interfere with the vortices produced by flapping, breaking down the reverse Kármán street and weakening the thrust jet.

We conclude that tubercles diminish performance in flapping foil propulsion. If tubercles are used on a flapping foil, it would be best to restrict flapping parameters to lightly loaded conditions where the performance difference is minimized.

Chapter 4

Summary and Conclusions

This thesis began by motivating the study of biologically inspired leading-edge tubercles. It has presented experimental results from two separate but complementary studies using tubercles on both static and dynamic foils. Key points from studies are summarized here before overall conclusions and recommendations are given.

4.1 Summary of Chapter Two: Static Foil Study

The static foil study compared the lift and drag characteristics of experimental hydrofoils with and without tubercles. The function and morphology of humpback whale pectoral flippers was discussed. Lift coefficient, C_L, and drag coefficient, C_D, were identified as the principal performance metrics for a control surface, and stall was discussed as an important limitation to the performance of a lifting surface. Reynolds number, R_e, was identified as an important parameter in determining what type of stall occurs. While previous studies have shown that tubercles delay leading edge stall, measurements presented here indicate that tubercles also delay trailing edge stall. Tubercles reduced the maximum lift in all tests except for the one at $R_e = 1.2 \times 10^5$, indicating that the effect of increased maximum lift that was observed in previous studies is dependent on stall type and other Reynolds number effects.

PIV flow visualization at $R_e = 8.9 \times 10^4$ showed flow separation at the trailing edge of both foils as attack angle was increased, confirming that the foils were in trailing

edge stall. Low velocity cells were identified downstream from the troughs between tubercles. Surface normal vorticity in the ensemble averaged flow fields showed distinct pairs of opposite sign vortical structures being generated by the tubercles. The suggested explanation of these structures was that they function analogous to the vortices shed from the leading edge of a delta wing, enhancing lift by suction.

4.2 Summary of Chapter Three: Dynamic Foil Study

Tubercles were used on a flapping foil for the first time in the dynamic foil study detailed in Chapter Three. The kinematics of two-dimensional and three-dimensional flapping were defined, and the reverse Kàrmàn street was introduced as the characteristic thrust producing flapping foil wake. The heave-to-chord ratio, $h_{0.7}/\bar{c}$, Strouhal number, S_t, and maximum attack angle, α_{max} were identified as the principal dimensionless parameters governing the structure of the wake. Previous studies on two-dimensional and three-dimensional flapping foils were summarized. The flapping foil actuator was introduced and experimental procedures were outlined.

Mean thrust coefficient, C_T, power coefficient, C_P, and efficiency, η, were measured over a broad parametric space using both foils. The trends in thrust and efficiency across flapping parameters are consistent with expectations from an understanding of how the parameters relate to the reverse Kàrmàn street . They are also consistent with trends observed in previous studies in the literature. On average, the tubercled test foil produced 6.22% less thrust while consuming 0.61% less power than the smooth control foil, and was therefore less efficient in flapping. The difference between the results using the two foils grew as loading was increased. The vortical structures generated by the tubercles are the likely reason for this decrease in performance.

Mean lift coefficient, C_L, and mean thrust coefficient were measured in maneuvering experiments using nonzero pitch bias. Again the test foil performed worse than the control foil in the majority of the tests, and again the difference grew as loading increased.

4.3 Conclusions and Recommendations

This thesis has opened the window to understanding the underlying physics behind tubercles. PIV measurements of the velocity field over a static foil with tubercles have been taken for the first time; they show that tubercles produce pairs of vortical structures that strengthen with increasing attack angle. Force measurements on a flapping foil with tubercles have been taken for the first time; they show that tubercles degrade performance in flapping. A likely explanation is that

- Energy that would normally go into generating the vortices in the reverse Kàrmàn street is used to generate the chordwise vortical structures.
- The thrust wake breaks down due to the interactions between the vortical structures generated by tubercles and those generated by flapping.

This explanation is reasonable because similar issues and end results are observed with the introduction of parasitic drag vortices generated by a corrupt attack angle profile. Three-dimensional tomographic PIV would probably be the most effective way to confirm this hypothesis, though several planes of two-dimensional PIV on a two-dimensional flapping foil with tubercles may also work.

It is a bit ironic, but it seems the same mechanism that improves performance when tubercles are used on a static foil actually degrades performance on a dynamic foil.

Tubercles are not recommended for use on flapping foils. They do show promise, however, for use on conventional control surfaces. Previous work and force measurements presented in the static study of this thesis indicate that tubercles are probably most advantageous in applications where leading edge stall is predominant. This suggests that they may be useful on thinner cross-section foils, which might be an interesting area to explore in future work. Two-dimensional PIV on other planes–particularly the plane normal to the flow–would also be illuminating. This could confirm the hypothesis that tubercles function analogous to delta wings with leading edge vortex rollup. Full three-dimensional tomographic PIV would also be a more effective tool to use in that study.

Coming full circle and returning to our biological inspiration, the findings of this thesis check out. If tubercles delay stall in static foils, it makes sense that the humpback whale has them on pectoral flippers that are used primarily as static hydroplanes. If tubercles degrade flapping foil performance, it makes sense that they are not found on the wings of birds and other animals that fly or swim by flapping their wings, fins, or flippers. It also makes sense that humpbacks do not have tubercles on their flukes. It seems that the most likely animal to evolve tubercles would have separate appendages for thrust and maneuvering, be large enough to have hydroplanes in the appropriate stall regime, and have a great need for agility. That animal is *Megaptera novæangilæ*.

Appendix A

Experimental Procedures and Details

A.1 Calibration and Methods

A.1.1 Force Sensor: AMTI MC1-6-250

The primary sensor for this thesis was the AMTI MC1-6-250 six-axis submersible dynamometer (Serial No. M4657, Advanced Mechanical Technology, Inc.). It uses a six full-bridge strain gauges oriented to provide force and moment measurements in sensor-referenced x, y, and z directions. The small size of this sensor allows mounting between the actuator and the foil, enabling direct measurements of power input to the foil, isolated from the electrical power input to the actuator. This may seem subtle, but is important, since the power will be used to determine the *hydrodynamic* efficiency of the *foil*, instead of the overall efficiency of the actuator and foil together.

The dynamometer has a small amount of crosstalk between channels and this must be accounted for in calibration and converting the measurement voltages to corresponding forces and moments. The factory-supplied calibration data shows less than 2% crosstalk on all channels. This can be a significant error in foil force measurements because forces being measured simultaneously can often by an order of magnitude or more. The factory provides a 6×6 sensitivity matrix that uses a least

squares fit and includes off-diagonal terms to account for crosstalk (without crosstalk, the matrix would simply be diagonal). A simple matrix equation converts measured voltages to corresponding forces.

$$\boldsymbol{F} = \bar{\boldsymbol{S}}^{-1}\boldsymbol{V} \tag{A.1}$$

The factory-supplied sensitivity matrix is:

$$\boldsymbol{S} = \begin{bmatrix} 1.5950 & -0.0593 & -0.0006 & 1.9692 & 0.7044 & 0.4699 \\ 0.0432 & 1.5973 & 0.0038 & -0.8275 & 0.3616 & -0.3531 \\ -0.0157 & -0.0111 & 0.3928 & 0.2311 & -0.7363 & -0.5341 \\ 0.0495 & 0.0083 & -0.0367 & 119.4688 & -0.3755 & -0.5390 \\ 0.0084 & 0.0000 & 0.0115 & 1.3831 & 120.9769 & -0.6633 \\ 0.0120 & 0.0249 & 0.0021 & 0.1549 & 0.1855 & 121.7679 \end{bmatrix} \tag{A.2}$$

and

$$\bar{\boldsymbol{S}} = \boldsymbol{S} \cdot \boldsymbol{G} \cdot V_{ex} \times 10^{-6} \tag{A.3}$$

when connected to the NI strain gauge driver, the gain vector is one, $\boldsymbol{G} = 1$. The six channels share a common excitation voltage, $V_{ex} = 10$.

McLetchie [16] and Lim [15] both used this sensor in previous studies. They performed full calibrations on all channels of the dynamometer and found close agreement with the factory-supplied matrix. Since the factory calibration is performed under closely controlled conditions and with many measurements across the entire operating range, Lim chose to use the factory supplied matrix. This thesis also uses the factory supplied matrix, which was nominally verified with principal axis measurements.

A.1.2 Potentiometers: Inscale GL200

Angular positions in roll and pitch are measured directly by shaft-mounted potentiometers. This eliminates gearhead and drivetrain backlash effects that would be present if the motor encoders were used. The potentiometers are powered and con-

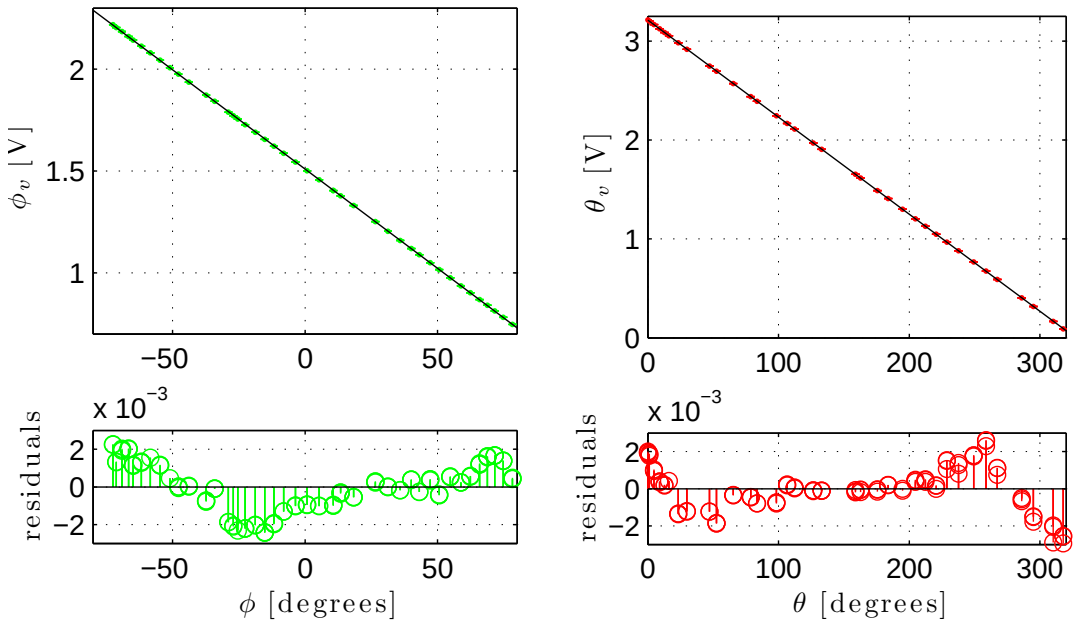

(a) Roll potentiometer

(b) Pitch potentiometer

Figure A-1
Calibration data and linear least squares fits for roll and pitch potentiometers. Mean measurements and 95% confidence bars are shown at each angle measured. The linear fit and its residuals are also shown.

ditioned through an excitation amplifier (SCXI-1120) on the DAQ chassis. They have a nominal resistance of 20 kΩ and 340° of electrical travel. They were bench-calibrated to determine the slope and linearity, using a digital protractor (SmartTool Technologies, Pro360) as ground truth. The zero positions are determined during the alignment of the AMTI sensor (see Appendix A.2).

The digital protractor was fixed to the output shaft and data recorded at several angles. The mean and variance of the signal for each angle provided a single data point and standard deviation for the calibration curve. The calibration slope and confidence was then computed using a robust linear least squares fit. Figure A-1 and Table A.1 summarize the calibration and results for both potentiometers.

Table A.1
Potentiometer calibration characteristics.

	slope [°/V]	sse	r^2	adj. r^2	rmse
ϕ (roll)	102.6	2.5662	1.00	1.00	0.1439
θ (pitch)	101.9	1.6256	1.00	1.00	0.1256

A.2 Alignment and Methods

A.2.1 Force sensor alignment

The force sensor needed to be aligned to laboratory coordinates so that an initial reference point was known. It was mounted to the output shaft of the actuator and moved to a vertical position, as measured by the digital protractor. The roll zero position was $\phi_v(0) = 1.5395$ V.

Alignment of the pitch axis was a more involved process. The actuator was mounted to the top window and aligned to its edges with a ruler before the collet on the mounting shaft was tightened. It was assumed that the offset box and top window were aligned with the tunnel. A pulley was positioned along the centerline of the tunnel (within 1 mm) at the height of the force sensor, approximately 600 mm behind it. A calibration weight was hung from the sensor over this pulley, with an estimated alignment error of < 0.002 degrees between the tunnel centerline and the direction of the force. The actuator was moved in small increments over its range, and the mean sensor-referenced forces and pitch potentiometer readings were recorded at each increment.

Data for X_s and M_s were plotted against pitch potentiometer voltage. Sine fits were applied to each using the robust trust-region reflective newton algorithm from the MATLAB curvefitting toolbox. Details of the fits are presented in Figure A-2 and Table A.2. The zero positions specified by the X_s channel and M_s channel differ by 0.16°; the value from the M_s channel is used because it is a stronger, cleaner signal and the goodness of fit indicators are better.

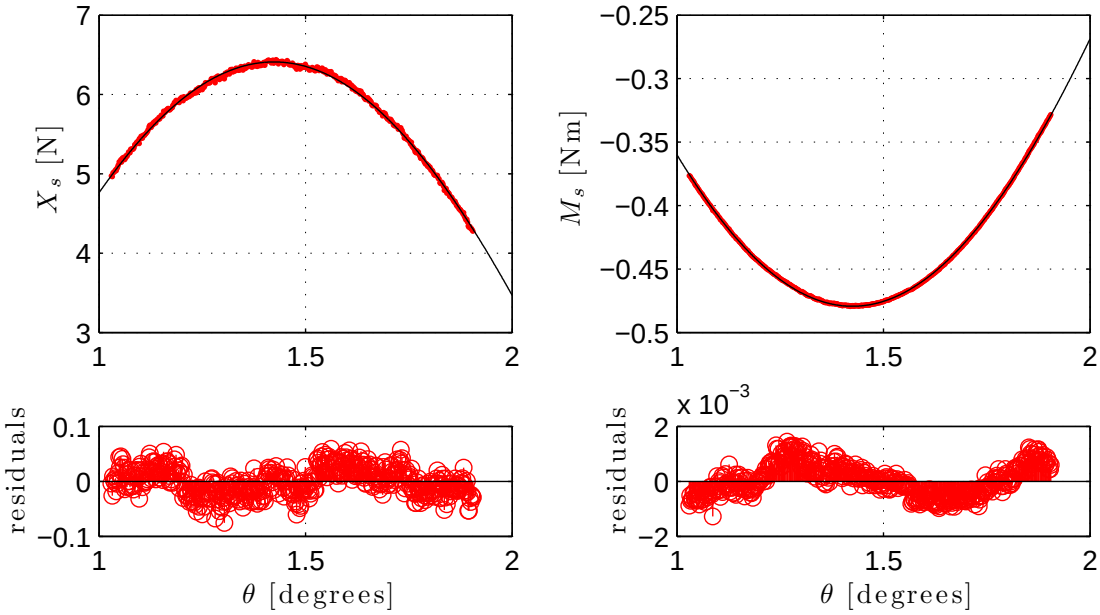

(a) (b)

Figure A-2
Pitch axis alignment data and sine fits for X_s and M_s channels. Mean measurements are shown at each angle measured. The sine fit and its residuals are also shown.

Table A.2
Pitch axis alignment sine fits of the form $a \sin(bx + c)$.

	X_s	M_s
a	6.41	0.4793
b	1.733	1.697
c	5.388	2.294
sse	0.3187	1.6232e-4
r^2	0.9979	0.9998
adj. r^2	0.9979	0.9998
rmse	0.0263	5.9402e-4
$\theta_v(0)$ [v]	1.4234	1.4250

A.2.2 Foil alignment

Any time a foil is mounted, tests must be performed to determine the misalignment between the force sensor and the foil. Repeated experiments are conducted varying the attack angle of the foil by half-degree increments within the initial linear lift range $-9^\circ < \alpha < 9^\circ$. These tests are conducted at 2.0 m/s tunnel speed, so that large forces are measured and sensor noise-related uncertainty is minimized. The lift curve is assumed to be symmetric across $\alpha = 0$ since both experimental hydrofoils have a symmetric, uncambered cross section.

The lift on the foil is computed starting with an initial assumed misalignment of $\epsilon_a = 0^\circ$. A linear least squares fit is applied to the data and the zero crossing of the fit, ϵ_i is recorded. This process iterates, adjusting the assumed misalignment as $\epsilon_a = \epsilon_{i-1} + \epsilon_i/3$, until the misalignment value converges within 0.0001°. Sets of experiments are repeated until there is good agreement between them, and a mean value is taken for the pitch zero position, $\theta_v(0)$, for that particular mounting of that foil. As stated previously, this procedure is repeated any time a foil is mounted to the apparatus.

The basic principle of this alignment procedure is the same as that used by Lim in [15], but the method is improved. Lim's method relied on the use of the external tunnel dynamometer, and therefore required more calibrations and involved more sensors. More importantly, it measured the total lift force on the foil and actuator, including all the associated cables and connectors. This force was observed as highly unsteady, due to the complicated flow internal to the fairing and around the actuator and cables. The method outlined here utilizes the AMTI sensor because it measures the forces on the foil, independent of the forces on those on the actuator. It also relies on a linear fit through several data points in each alignment, and should be more reliable based solely on that fact.

A.3 Troubleshooting

A.3.1 Ground Loop

One problem Lim [15] encountered in his experiments using this actuator in the MHL water tunnel was a ground loop that caused a DC shift in the raw voltage outputs on all six channels of the AMTI force sensor. After connecting some of his other sensors to batteries, he determined that the DC shift was toggled by the motor power supplies and by resetting the encoder counts, but that they appeared to return to original levels once the motors were put in motion. Despite his efforts, he was unable to isolate the problem any further during his research.

Lim's setup was replicated at the beginning of these experiments, and the same DC shift was observed, but signals never appeared to return to normal levels with motor motion. The ground loop situation was unacceptable for continuing experiments with this apparatus, so it had to be isolated and eliminated. The motor drivers were replaced with a new two-axis controller and integrated power supply/servomotor drive (National Instruments, PXI-7352 and MID-7652). This improvement also allowed better integration between actuation and data acquisition. Any time the motors were energized, the AMTI signals shifted as before. The AMTI MCA-6 signal conditioner/amplifier was eventually identified as the source of the ground loop problem. Ground loop effects were eliminated once the force sensor excitation was moved to an independent external power supply. The microvolt-level signals were then wired into a universal strain gauge excitation amplifier (National Instruments, SCXI-1520) mounted in the DAQ chassis. All power for the motor driver, sensors, and signal acquisition devices was supplied through the same isolator/conditioner (Kleenline, ISO/T-34). In this configuration, force sensor outputs were unaffected by the state of the motors, and the ground loop was eliminated.

A.3.2 Encoder signal conditioning

With the new motor drivers, the encoder signals were corrupted by high-amplitude, high-frequency EMI noise produced by the motor PWM cycles, despite being on a separate bulkhead connectors. This would cause lost counts in the control signals, and the roll and pitch axes would creep slowly from their initial positions. In general, this was not a major problem except when running the actuator for a long time or under high loads, but it was a source of error and annoyance during experiments.

The actuator was rewired to place all encoder signals on coaxial cable to increase EMI rejection. The signal voltages were also level-shifted using standard RS-232 tranceiver ICs. This increased the signal immunity to EMI by changing the original 0-2.4 VDC encoder outputs to ±12 VDC. These encoder signal conditioners, seen in Figure A-3, eliminated the lost encoder count problem and improved the experimental apparatus, giving it repeatable motion without any dependence on running time or actuator load.

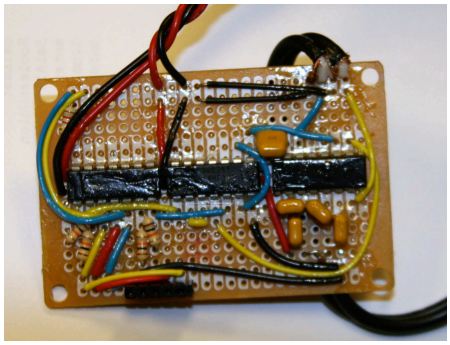

Figure A-3
Photograph of one of the encoder signal conditioners used to eliminate the motor creeping problem.

Appendix B

Complete Dynamic Results

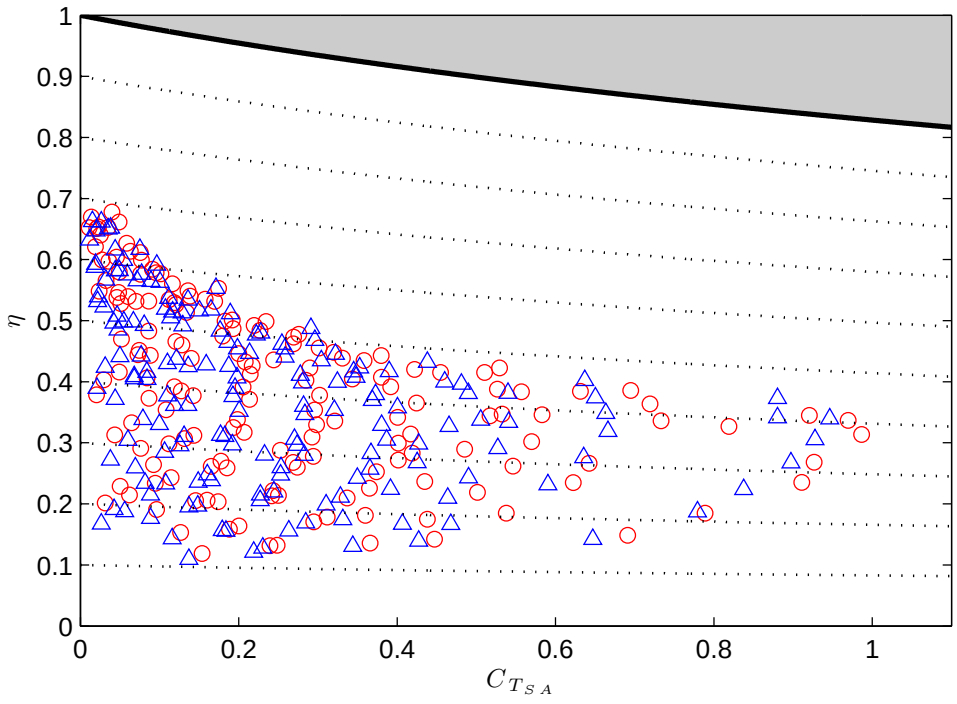

Figure B-1
Swept area thrust coefficient versus hydrodynamic efficiency for smooth control foil (○) and tubercled test foil (△). The thick line at the top of the plot denotes the maximum efficiency possible with an ideal thruster (actuator disk). Dotted lines below indicate 90% to 10% of ideal efficiency.

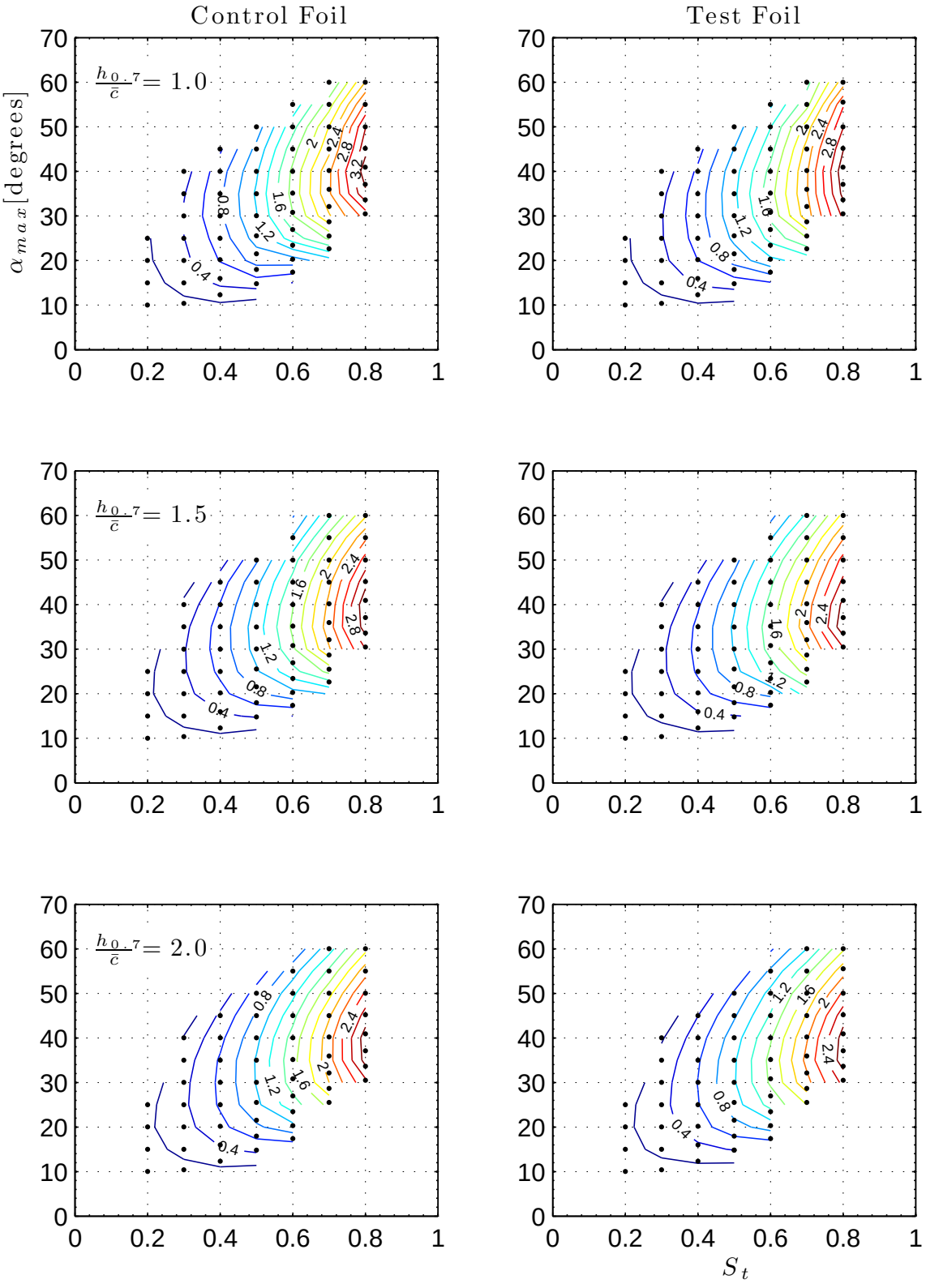

Figure B-2
Contours of thrust coefficient for both foils.

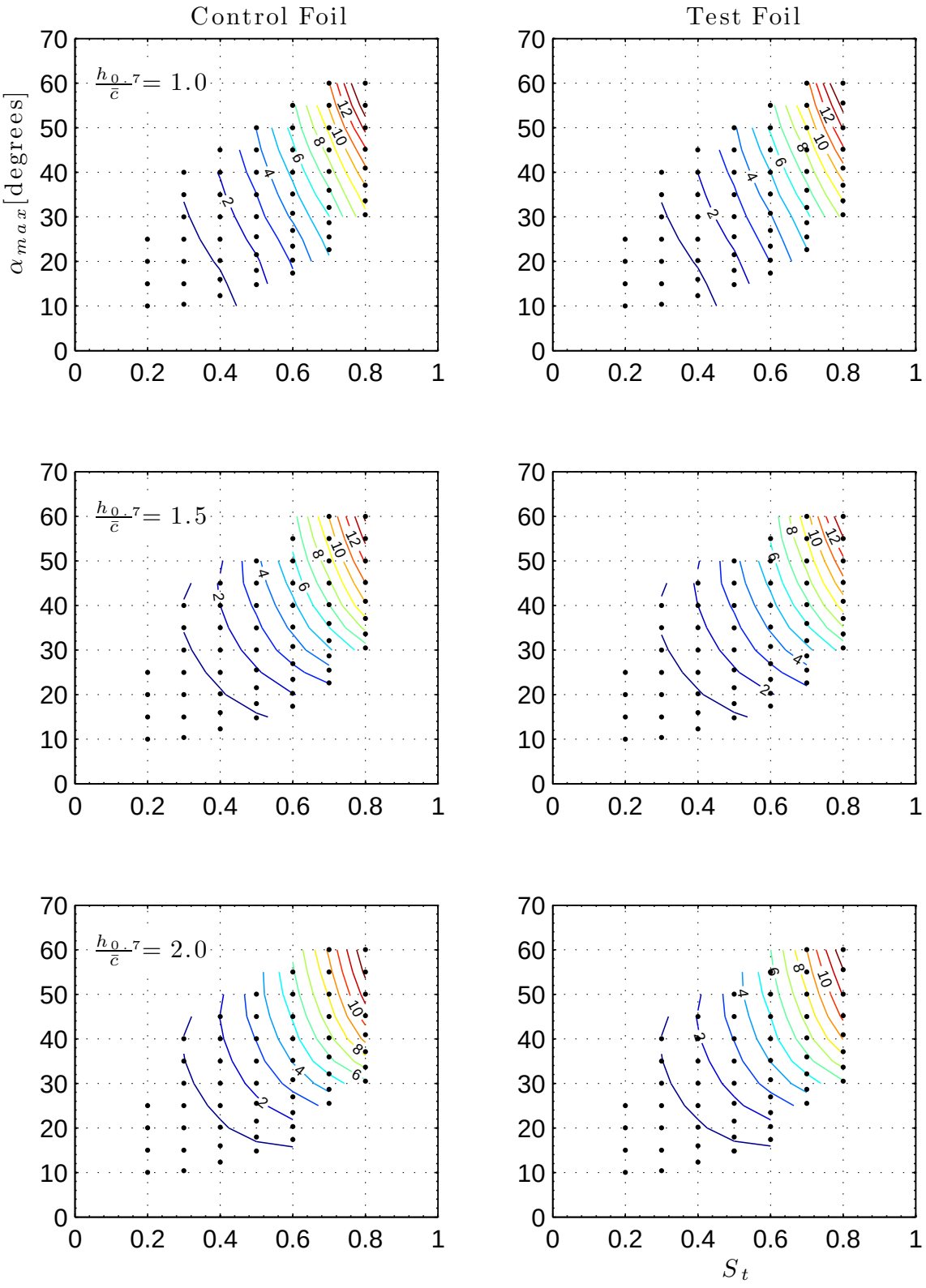

Figure B-3
Contours of power coefficient for both foils.

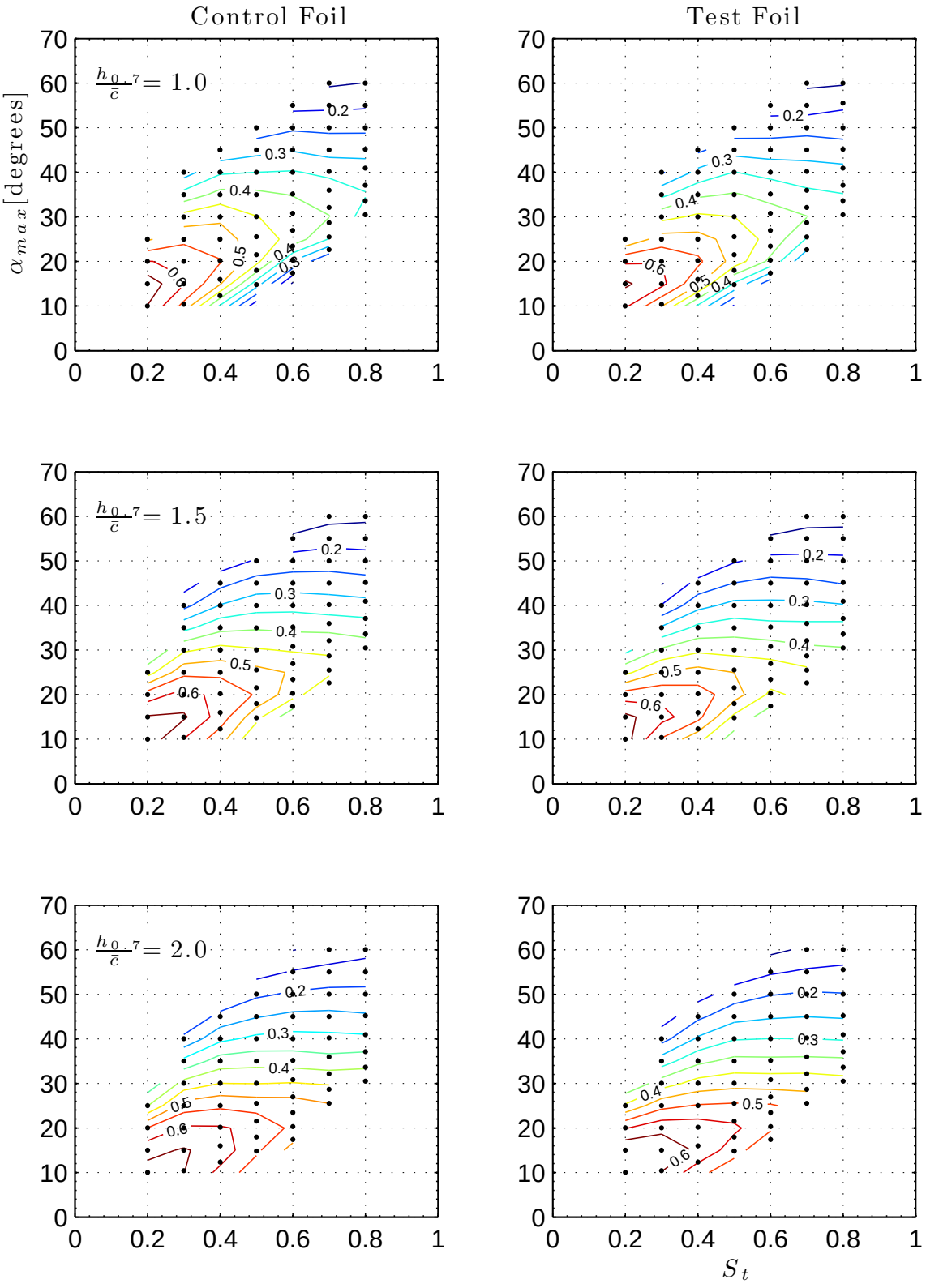

Figure B-4
Contours of efficiency for both foils.

Table B.1
Flap parameters and coefficients for thrust production tests at $h_{0.7}/\bar{c} = 1.0$ using smooth foil.

S_t	α_{max}	C_T	C_P	η	$C_{T_{SA}}$	η/η_i
0.20	10.0°	0.079	0.123	0.639	0.023	0.643
	15.0°	0.140	0.203	0.689	0.040	0.696
	20.0°	0.177	0.296	0.599	0.051	0.606
	25.0°	0.189	0.388	0.487	0.054	0.494
0.30	10.4°	0.162	0.296	0.545	0.046	0.551
	15.0°	0.263	0.432	0.608	0.075	0.619
	20.0°	0.340	0.576	0.591	0.098	0.605
	25.0°	0.390	0.723	0.539	0.112	0.554
	30.0°	0.425	0.895	0.475	0.122	0.489
	35.0°	0.383	1.052	0.364	0.110	0.374
	40.0°	0.327	1.208	0.271	0.093	0.277
0.40	12.3°	0.288	0.722	0.399	0.083	0.407
	16.0°	0.486	0.900	0.540	0.139	0.558
	20.2°	0.607	1.103	0.550	0.173	0.573
	25.0°	0.680	1.333	0.510	0.195	0.534
	30.0°	0.780	1.552	0.503	0.223	0.529
	35.0°	0.760	1.816	0.419	0.217	0.440
	40.0°	0.718	2.043	0.351	0.205	0.368
	45.0°	0.578	2.215	0.261	0.164	0.271
0.50	14.8°	0.505	1.628	0.311	0.144	0.321
	18.0°	0.747	1.769	0.422	0.216	0.444
	21.5°	0.982	2.011	0.488	0.281	0.520
	25.5°	1.075	2.307	0.466	0.308	0.499
	30.0°	1.172	2.630	0.446	0.337	0.480
	35.0°	1.222	2.965	0.412	0.351	0.445
	40.0°	1.152	3.329	0.346	0.330	0.373
	45.0°	1.031	3.685	0.280	0.296	0.299
	50.0°	0.889	4.088	0.218	0.253	0.230
0.60	17.4°	0.602	3.001	0.201	0.174	0.209
	20.3°	0.891	3.075	0.290	0.257	0.307
	23.4°	1.361	3.257	0.418	0.392	0.455
	26.9°	1.610	3.801	0.424	0.466	0.468
	30.8°	1.809	4.302	0.420	0.512	0.469
	35.1°	1.872	4.731	0.396	0.536	0.443
	40.0°	1.863	5.226	0.357	0.533	0.399

...continued on next page

Table B.1
(continued from previous page) Flap parameters and coefficients for thrust production tests at $h_{0.7}/\bar{c} = 1.0$ using smooth foil.

S_t	α_{max}	C_T	C_P	η	$C_{T_{SA}}$	η/η_i
	45.0°	1.743	5.836	0.299	0.501	0.332
	50.0°	1.548	6.315	0.245	0.445	0.270
	55.0°	1.264	6.767	0.187	0.360	0.202
0.70	22.6°	1.483	5.241	0.283	0.424	0.310
	25.5°	1.880	5.382	0.349	0.544	0.392
	28.7°	2.268	5.722	0.396	0.653	0.453
	32.1°	2.451	6.258	0.392	0.706	0.452
	35.9°	2.550	6.872	0.371	0.733	0.430
	40.2°	2.543	7.549	0.337	0.733	0.390
	45.0°	2.278	8.303	0.274	0.656	0.314
	50.0°	2.198	9.150	0.240	0.633	0.274
	55.0°	1.881	10.070	0.187	0.540	0.209
	60.0°	1.554	10.863	0.143	0.443	0.158
0.80	30.5°	2.916	8.882	0.328	0.830	0.386
	33.6°	3.234	9.286	0.348	0.936	0.416
	37.1°	3.427	10.051	0.341	0.982	0.410
	40.9°	3.532	10.937	0.323	1.014	0.391
	45.2°	3.308	11.906	0.278	0.950	0.333
	50.0°	3.223	13.355	0.241	0.928	0.288
	55.0°	2.840	14.778	0.192	0.818	0.226
	60.0°	2.413	15.984	0.151	0.689	0.174

Table B.2
Flap parameters and coefficients for thrust production tests at $h_{0.7}/\bar{c} = 1.5$ using smooth foil.

S_t	α_{max}	C_T	C_P	η	$C_{T_{SA}}$	η/η_i
0.20	10.0°	0.074	0.109	0.680	0.014	0.682
	15.0°	0.135	0.207	0.652	0.026	0.656
	20.0°	0.176	0.304	0.579	0.033	0.583
	25.0°	0.158	0.384	0.413	0.030	0.416
0.30	10.4°	0.144	0.242	0.596	0.027	0.600
	15.0°	0.264	0.393	0.671	0.050	0.679
	20.0°	0.341	0.546	0.625	0.064	0.635
	25.0°	0.380	0.700	0.543	0.072	0.552
	30.0°	0.386	0.864	0.447	0.073	0.455
	35.0°	0.347	1.036	0.335	0.065	0.341
	40.0°	0.265	1.165	0.228	0.050	0.231
0.40	12.3°	0.258	0.468	0.551	0.049	0.558
	16.0°	0.407	0.702	0.579	0.077	0.590
	20.2°	0.539	0.930	0.579	0.101	0.593
	25.0°	0.636	1.186	0.537	0.120	0.552
	30.0°	0.683	1.466	0.466	0.129	0.480
	35.0°	0.683	1.752	0.390	0.129	0.402
	40.0°	0.603	1.984	0.304	0.113	0.312
	45.0°	0.506	2.134	0.237	0.095	0.243
0.50	14.8°	0.394	0.874	0.450	0.075	0.459
	18.0°	0.651	1.233	0.528	0.121	0.544
	21.5°	0.843	1.551	0.543	0.160	0.564
	25.5°	0.976	1.939	0.503	0.184	0.525
	30.0°	1.072	2.377	0.451	0.202	0.473
	35.0°	1.094	2.767	0.395	0.206	0.415
	40.0°	1.031	3.149	0.327	0.195	0.343
	45.0°	0.956	3.484	0.275	0.180	0.286
	50.0°	0.778	3.775	0.206	0.146	0.213
0.60	17.4°	0.629	1.606	0.392	0.120	0.403
	20.3°	0.969	2.000	0.484	0.183	0.506
	23.5°	1.207	2.482	0.486	0.229	0.513
	26.9°	1.453	3.008	0.483	0.275	0.514
	30.8°	1.556	3.639	0.428	0.294	0.457
	35.1°	1.643	4.228	0.389	0.310	0.417
	40.0°	1.595	4.769	0.334	0.301	0.358

...continued on next page

Table B.2
(continued from previous page) Flap parameters and coefficients for thrust production tests at $h_{0.7}/\bar{c} = 1.5$ using smooth foil.

S_t	α_{max}	C_T	C_P	η	$C_{T_{SA}}$	η/η_i
	45.0°	1.450	5.315	0.273	0.274	0.290
	50.0°	1.320	5.825	0.227	0.248	0.240
	55.0°	0.997	6.238	0.160	0.188	0.167
0.70	22.6°	1.297	2.979	0.436	0.246	0.461
	25.5°	1.715	3.745	0.458	0.326	0.493
	28.7°	2.049	4.546	0.451	0.387	0.491
	32.1°	2.271	5.315	0.427	0.429	0.469
	35.9°	2.269	6.132	0.370	0.429	0.406
	40.2°	2.226	6.963	0.320	0.420	0.350
	45.0°	2.151	7.774	0.277	0.406	0.302
	50.0°	1.950	8.575	0.227	0.368	0.247
	55.0°	1.686	9.273	0.182	0.317	0.195
	60.0°	1.349	10.006	0.135	0.252	0.143
0.80	30.5°	2.860	6.692	0.427	0.538	0.479
	33.6°	2.976	7.654	0.389	0.562	0.437
	37.1°	3.167	9.036	0.351	0.594	0.397
	40.9°	3.106	10.076	0.308	0.584	0.348
	45.2°	2.927	11.038	0.265	0.551	0.298
	50.0°	2.688	12.173	0.221	0.505	0.246
	55.0°	2.364	13.319	0.177	0.445	0.195
	60.0°	1.967	14.237	0.138	0.368	0.150

Table B.3
Flap parameters and coefficients for thrust production tests at $h_{0.7}/\bar{c} = 2.0$ using smooth foil.

S_t	α_{max}	C_T	C_P	η	$C_{T_{SA}}$	η/η_i
0.20	10.0°	0.080	0.121	0.664	0.011	0.665
	15.0°	0.138	0.218	0.635	0.020	0.638
	20.0°	0.171	0.307	0.556	0.024	0.559
	25.0°	0.147	0.383	0.382	0.021	0.384
0.30	10.4°	0.145	0.222	0.653	0.021	0.657
	15.0°	0.250	0.379	0.660	0.035	0.666
	20.0°	0.329	0.536	0.612	0.046	0.620
	25.0°	0.367	0.688	0.533	0.052	0.540
	30.0°	0.351	0.835	0.420	0.049	0.425
	35.0°	0.309	0.983	0.315	0.043	0.318
	40.0°	0.223	1.101	0.203	0.031	0.204
0.40	12.3°	0.257	0.430	0.597	0.036	0.603
	16.0°	0.419	0.659	0.635	0.059	0.645
	20.2°	0.546	0.913	0.597	0.077	0.609
	25.0°	0.622	1.153	0.540	0.088	0.551
	30.0°	0.633	1.413	0.448	0.089	0.458
	35.0°	0.624	1.652	0.378	0.088	0.386
	40.0°	0.545	1.858	0.293	0.077	0.299
	45.0°	0.445	2.061	0.216	0.062	0.219
0.50	14.8°	0.443	0.805	0.550	0.062	0.559
	40.0°	0.945	3.040	0.311	0.133	0.321
	45.0°	0.823	3.349	0.246	0.116	0.253
	18.0°	0.652	1.099	0.593	0.092	0.606
	21.5°	0.833	1.469	0.567	0.117	0.583
	25.5°	0.963	1.853	0.520	0.135	0.537
	30.0°	1.005	2.266	0.443	0.141	0.458
	35.0°	1.017	2.673	0.381	0.143	0.394
	50.0°	0.693	3.591	0.193	0.097	0.198
0.60	17.4°	0.620	1.267	0.489	0.088	0.500
	45.0°	1.329	5.076	0.262	0.187	0.274
	50.0°	1.143	5.526	0.207	0.160	0.215
	55.0°	0.908	5.876	0.155	0.127	0.159
	20.3°	0.968	1.765	0.548	0.136	0.566
	23.5°	1.216	2.252	0.540	0.172	0.562
	35.1°	1.528	4.088	0.374	0.215	0.393

...continued on next page

Table B.3
(continued from previous page) Flap parameters and coefficients for thrust production tests at $h_{0.7}/\bar{c} = 2.0$ using smooth foil.

S_t	α_{max}	C_T	C_P	η	$C_{T_{SA}}$	η/η_i
	40.0°	1.483	4.643	0.320	0.209	0.335
	26.9°	1.386	2.808	0.494	0.195	0.517
	30.8°	1.509	3.419	0.441	0.212	0.464
0.70	25.5°	1.683	3.333	0.505	0.238	0.533
	28.7°	1.922	4.143	0.464	0.270	0.494
	32.1°	2.042	5.034	0.406	0.287	0.433
	36.0°	2.108	5.948	0.354	0.296	0.379
	40.2°	2.104	6.701	0.314	0.296	0.336
	45.0°	1.969	7.493	0.263	0.276	0.280
	50.0°	1.738	8.067	0.215	0.244	0.228
	55.0°	1.430	8.648	0.165	0.201	0.173
	60.0°	1.106	9.161	0.121	0.155	0.125
0.80	30.5°	2.567	5.862	0.438	0.361	0.474
	33.6°	2.806	7.048	0.398	0.397	0.434
	37.1°	2.884	8.340	0.346	0.405	0.378
	40.9°	2.880	9.528	0.302	0.405	0.330
	45.2°	2.671	10.524	0.254	0.375	0.276
	50.0°	2.441	11.437	0.213	0.344	0.230
	55.0°	2.117	12.273	0.172	0.298	0.184
	60.0°	1.745	12.914	0.135	0.245	0.143

Table B.4
Flap parameters and coefficients for thrust production tests at $h_{0.7}/\bar{c} = 1.0$ using tubercle foil.

S_t	α_{max}	C_T	C_P	η	$C_{T_{SA}}$	η/η_i
0.20	10.0°	0.068	0.113	0.601	0.019	0.604
	15.0°	0.135	0.203	0.664	0.039	0.670
	20.0°	0.175	0.294	0.593	0.050	0.601
	25.0°	0.176	0.394	0.447	0.050	0.453
0.30	10.4°	0.150	0.293	0.512	0.043	0.518
	15.0°	0.265	0.423	0.626	0.076	0.638
	20.0°	0.342	0.570	0.600	0.098	0.614
	25.0°	0.381	0.724	0.527	0.109	0.541
	30.0°	0.391	0.896	0.436	0.111	0.448
	35.0°	0.356	1.055	0.338	0.102	0.346
	40.0°	0.292	1.236	0.237	0.082	0.241
0.40	12.3°	0.296	0.731	0.405	0.084	0.413
	16.0°	0.482	0.886	0.544	0.138	0.562
	20.2°	0.605	1.082	0.559	0.173	0.582
	25.0°	0.668	1.300	0.514	0.190	0.538
	30.0°	0.703	1.528	0.460	0.201	0.482
	35.0°	0.692	1.758	0.394	0.198	0.413
	40.0°	0.625	1.982	0.315	0.178	0.329
	45.0°	0.529	2.214	0.239	0.150	0.247
0.50	14.8°	0.466	1.481	0.315	0.133	0.325
	18.0°	0.761	1.679	0.453	0.217	0.476
	21.5°	0.903	1.924	0.469	0.260	0.498
	25.5°	1.052	2.215	0.475	0.300	0.508
	30.0°	1.144	2.537	0.451	0.326	0.485
	35.0°	1.151	2.849	0.404	0.329	0.435
	40.0°	1.139	3.193	0.357	0.324	0.384
	45.0°	1.007	3.554	0.283	0.286	0.302
	50.0°	0.871	3.880	0.224	0.246	0.238
0.60	17.4°	0.821	2.894	0.284	0.237	0.300
	20.3°	1.233	2.988	0.413	0.354	0.447
	23.5°	1.378	3.285	0.419	0.392	0.457
	26.9°	1.551	3.581	0.433	0.440	0.477
	30.8°	1.633	4.018	0.407	0.469	0.450
	35.1°	1.745	4.513	0.387	0.498	0.430
	40.0°	1.653	4.995	0.331	0.472	0.366

...continued on next page

Table B.4
(continued from previous page) Flap parameters and coefficients for thrust production tests at $h_{0.7}/\bar{c} = 1.0$ using tubercle foil.

S_t	α_{max}	C_T	C_P	η	$C_{T_{SA}}$	η/η_i
	45.0°	1.509	5.579	0.271	0.431	0.297
	50.0°	1.393	6.166	0.226	0.396	0.246
	55.0°	1.182	6.671	0.177	0.335	0.191
0.70	22.6°	1.510	5.069	0.298	0.425	0.327
	25.5°	1.782	5.241	0.340	0.512	0.379
	28.7°	2.256	5.538	0.407	0.648	0.465
	32.1°	2.310	6.125	0.377	0.660	0.432
	35.9°	2.345	6.702	0.350	0.670	0.401
	40.2°	2.361	7.353	0.321	0.673	0.368
	45.0°	2.261	8.077	0.280	0.647	0.320
	50.0°	2.107	8.914	0.236	0.602	0.268
	55.0°	1.663	9.834	0.169	0.476	0.187
	60.0°	1.522	10.537	0.145	0.433	0.159
0.80	30.5°	3.125	8.384	0.373	0.884	0.442
	33.6°	3.120	8.993	0.347	0.898	0.412
	37.1°	3.361	9.838	0.342	0.957	0.410
	40.9°	3.293	10.719	0.307	0.935	0.367
	45.2°	3.188	11.888	0.268	0.905	0.319
	50.0°	2.984	13.162	0.227	0.850	0.268
	55.5°	2.777	14.579	0.191	0.791	0.223
	60.0°	2.296	15.937	0.144	0.653	0.165

Table B.5
Flap parameters and coefficients for thrust production tests at $h_{0.7}/\bar{c} = 1.5$ using tubercle foil.

S_t	α_{max}	C_T	C_P	η	$C_{T_{SA}}$	η/η_i
0.20	10.0°	0.081	0.120	0.671	0.015	0.674
	15.0°	0.141	0.212	0.668	0.027	0.673
	20.0°	0.173	0.301	0.575	0.033	0.580
	25.0°	0.168	0.392	0.429	0.032	0.433
0.30	10.4°	0.116	0.214	0.540	0.022	0.543
	15.0°	0.234	0.375	0.624	0.044	0.631
	20.0°	0.317	0.543	0.583	0.060	0.592
	25.0°	0.359	0.711	0.505	0.068	0.513
	30.0°	0.365	0.890	0.411	0.069	0.418
	35.0°	0.323	1.052	0.307	0.061	0.312
	40.0°	0.229	1.189	0.193	0.043	0.195
0.40	12.3°	0.246	0.480	0.513	0.046	0.519
	16.0°	0.412	0.704	0.585	0.078	0.596
	20.2°	0.538	0.945	0.570	0.101	0.584
	25.0°	0.624	1.201	0.519	0.117	0.534
	30.0°	0.651	1.476	0.441	0.123	0.454
	35.0°	0.641	1.753	0.366	0.121	0.377
	40.0°	0.572	1.981	0.289	0.108	0.296
	45.0°	0.476	2.194	0.217	0.089	0.222
0.50	14.8°	0.364	0.874	0.416	0.069	0.423
	18.0°	0.611	1.199	0.510	0.115	0.524
	21.5°	0.804	1.544	0.521	0.151	0.540
	25.5°	0.944	1.933	0.488	0.178	0.509
	30.0°	1.002	2.354	0.426	0.187	0.445
	35.0°	1.035	2.728	0.379	0.194	0.397
	40.0°	0.980	3.114	0.315	0.185	0.329
	45.0°	0.861	3.445	0.250	0.162	0.260
	50.0°	0.736	3.737	0.197	0.138	0.203
0.60	23.5°	1.189	2.483	0.479	0.223	0.504
	26.9°	1.384	2.998	0.462	0.262	0.490
	30.8°	1.484	3.589	0.414	0.279	0.441
	35.1°	1.508	4.156	0.363	0.284	0.387
	40.0°	1.451	4.681	0.310	0.273	0.330
	45.0°	1.359	5.179	0.262	0.256	0.278
	50.0°	1.221	5.619	0.217	0.230	0.229

...continued on next page

Table B.5
(continued from previous page) Flap parameters and coefficients for thrust production tests at $h_{0.7}/\bar{c} = 1.5$ using tubercle foil.

S_t	α_{max}	C_T	C_P	η	$C_{T_{SA}}$	η/η_i
	55.0°	0.964	6.109	0.158	0.180	0.165
	17.4°	0.588	1.538	0.382	0.111	0.393
	20.3°	0.848	1.955	0.434	0.161	0.450
0.70	22.6°	1.569	3.170	0.495	0.296	0.529
	25.5°	1.629	3.708	0.439	0.307	0.471
	28.7°	1.886	4.409	0.428	0.357	0.463
	32.1°	1.996	5.237	0.381	0.376	0.414
	35.9°	2.147	5.943	0.361	0.405	0.395
	40.2°	2.075	6.737	0.308	0.392	0.336
	45.0°	1.958	7.569	0.259	0.368	0.281
	50.0°	1.762	8.277	0.213	0.331	0.229
	55.0°	1.529	8.972	0.170	0.287	0.182
	60.0°	1.234	9.550	0.129	0.231	0.136
0.80	30.5°	2.578	6.510	0.396	0.482	0.439
	33.6°	2.899	7.482	0.387	0.549	0.435
	37.1°	2.895	8.632	0.335	0.544	0.376
	40.9°	2.827	9.640	0.293	0.532	0.328
	45.2°	2.628	10.723	0.245	0.494	0.272
	50.0°	2.492	11.788	0.211	0.469	0.234
	55.0°	2.182	12.989	0.168	0.409	0.184
	60.0°	1.857	14.132	0.131	0.346	0.142

Table B.6
Flap parameters and coefficients for thrust production tests at $h_{0.7}/\bar{c} = 2.0$ using tubercle foil.

S_t	α_{max}	C_T	C_P	η	$C_{T_{SA}}$	η/η_i
0.20	10.0°	0.082	0.129	0.638	0.012	0.640
	15.0°	0.142	0.217	0.655	0.020	0.658
	20.0°	0.163	0.300	0.545	0.023	0.548
	25.0°	0.150	0.381	0.394	0.021	0.396
0.30	25.0°	0.340	0.692	0.491	0.048	0.497
	30.0°	0.316	0.841	0.376	0.044	0.380
	10.4°	0.134	0.223	0.600	0.019	0.603
	15.0°	0.251	0.381	0.660	0.035	0.665
	20.0°	0.317	0.538	0.589	0.045	0.595
	35.0°	0.273	0.992	0.275	0.038	0.278
	40.0°	0.190	1.120	0.170	0.027	0.171
0.40	12.3°	0.211	0.399	0.528	0.030	0.532
	16.0°	0.390	0.639	0.611	0.055	0.619
	20.2°	0.513	0.897	0.572	0.072	0.582
	25.0°	0.577	1.160	0.497	0.081	0.507
	30.0°	0.602	1.433	0.420	0.085	0.429
	35.0°	0.567	1.656	0.342	0.080	0.349
	40.0°	0.499	1.908	0.261	0.070	0.266
	45.0°	0.404	2.131	0.190	0.057	0.192
0.50	14.8°	0.408	0.781	0.522	0.057	0.530
	18.0°	0.638	1.116	0.571	0.090	0.584
	21.5°	0.801	1.469	0.546	0.113	0.561
	25.5°	0.927	1.868	0.496	0.130	0.512
	30.0°	0.978	2.278	0.429	0.137	0.443
	35.0°	0.976	2.674	0.365	0.137	0.377
	50.0°	0.636	3.583	0.178	0.089	0.182
	14.8°	0.393	0.772	0.508	0.056	0.515
	40.0°	0.906	3.026	0.299	0.128	0.309
	45.0°	0.774	3.294	0.235	0.108	0.241
0.60	20.3°	0.918	1.774	0.517	0.129	0.534
	23.5°	1.182	2.253	0.525	0.167	0.546
	35.1°	1.443	4.053	0.356	0.203	0.373
	40.0°	1.379	4.602	0.300	0.194	0.313
	26.9°	1.337	2.856	0.468	0.187	0.489
	30.8°	1.420	3.454	0.411	0.200	0.431

...continued on next page

Table B.6
(continued from previous page) Flap parameters and coefficients for thrust production tests at $h_{0.7}/\bar{c} = 2.0$ using tubercle foil.

S_t	α_{max}	C_T	C_P	η	$C_{T_{SA}}$	η/η_i
	17.4°	0.549	1.220	0.450	0.078	0.458
	45.0°	1.189	4.945	0.241	0.167	0.250
	50.0°	1.066	5.368	0.198	0.149	0.206
	55.0°	0.834	5.774	0.144	0.117	0.149
0.70	25.5°	1.633	3.376	0.484	0.229	0.510
	28.7°	1.856	4.160	0.446	0.261	0.474
	32.1°	2.016	5.021	0.402	0.283	0.428
	36.0°	2.035	5.829	0.349	0.286	0.373
	40.2°	1.966	6.599	0.298	0.276	0.317
	45.0°	1.817	7.277	0.250	0.255	0.265
	50.0°	1.634	7.873	0.208	0.229	0.219
	55.0°	1.320	8.416	0.157	0.185	0.164
	60.0°	0.984	8.895	0.111	0.138	0.114
0.80	30.5°	2.474	5.916	0.418	0.346	0.452
	33.6°	2.642	7.059	0.374	0.372	0.406
	37.1°	2.731	8.262	0.331	0.383	0.360
	40.9°	2.635	9.243	0.285	0.370	0.309
	45.2°	2.519	10.307	0.244	0.354	0.264
	50.0°	2.233	11.125	0.201	0.314	0.215
	55.5°	1.895	12.022	0.158	0.266	0.167
	60.0°	1.576	12.873	0.122	0.221	0.129

Table B.7
Reynolds number test case I: $h_{0.7}/\bar{c} = 1.5$, $S_t = 0.3$, $\alpha_{max} = 15.0$.

		smooth			tubercle		
R_e		C_T	C_P	η	C_T	C_P	η
17859	run 1	0.231	0.360	0.643	0.253	0.372	0.682
	run 2	0.274	0.356	0.772	0.244	0.374	0.654
	run 3	0.178	0.369	0.483	0.253	0.372	0.679
	mean	0.228	0.361	0.633	0.250	0.372	0.672
	std	0.048	0.007	0.145	0.005	0.001	0.016
	range	0.097	0.013	0.289	0.009	0.002	0.029
20836	run 1	0.277	0.370	0.747	0.266	0.381	0.698
	run 2	0.274	0.372	0.736	0.284	0.378	0.753
	run 3	0.253	0.375	0.675	0.272	0.382	0.714
	mean	0.268	0.372	0.719	0.274	0.380	0.722
	std	0.013	0.002	0.039	0.009	0.002	0.028
	range	0.024	0.005	0.072	0.019	0.004	0.055
23812	run 1	0.261	0.378	0.691	0.270	0.377	0.718
	run 2	0.252	0.379	0.665	0.246	0.384	0.642
	run 3	0.252	0.377	0.669	0.260	0.379	0.687
	mean	0.255	0.378	0.675	0.259	0.380	0.682
	std	0.005	0.001	0.014	0.012	0.004	0.038
	range	0.009	0.002	0.026	0.024	0.007	0.076
26788	run 1	0.239	0.381	0.627	0.273	0.393	0.695
	run 2	0.236	0.384	0.614	0.275	0.390	0.706
	run 3	0.268	0.385	0.696	0.262	0.393	0.667
	mean	0.248	0.384	0.646	0.270	0.392	0.689
	std	0.018	0.002	0.044	0.007	0.002	0.020
	range	0.032	0.004	0.081	0.014	0.003	0.040
29765	run 1	0.255	0.387	0.659	0.267	0.398	0.672
	run 2	0.237	0.395	0.600	0.258	0.399	0.648
	run 3	0.267	0.388	0.688	0.275	0.399	0.690
	mean	0.253	0.390	0.649	0.267	0.399	0.670
	std	0.015	0.005	0.045	0.008	0.000	0.021
	range	0.029	0.008	0.088	0.017	0.001	0.043
32742	run 1	0.266	0.390	0.683	0.266	0.397	0.671
	run 2	0.247	0.391	0.633	0.273	0.398	0.686
	run 3	0.261	0.392	0.667	0.256	0.393	0.651

...continued on next page

Table B.7
(continued from previous page) Reynolds number test case I: $h_{0.7}/\bar{c} = 1.5$, $S_t = 0.3$, $\alpha_{max} = 15.0$.

R_e		C_T	C_P	η	C_T	C_P	η
	mean	0.258	0.391	0.661	0.265	0.396	0.669
	std	0.010	0.001	0.026	0.008	0.002	0.018
	range	0.019	0.002	0.050	0.017	0.004	0.035
35718	run 1	0.266	0.389	0.683	0.282	0.394	0.717
	run 2	0.258	0.394	0.655	0.273	0.396	0.689
	run 3	0.262	0.396	0.661	0.267	0.395	0.676
	mean	0.262	0.393	0.666	0.274	0.395	0.694
	std	0.004	0.004	0.015	0.008	0.001	0.021
	range	0.008	0.007	0.029	0.015	0.002	0.041

Table B.8
Reynolds number test case II: $h_{0.7}/\bar{c} = 2.0$, $S_t = 0.3$, $\alpha_{max} = 15.0$.

		smooth			tubercle		
R_e		C_T	C_P	η	C_T	C_P	η
17859	run 1	0.209	0.359	0.583	0.246	0.371	0.664
	run 2	0.247	0.354	0.698	0.313	0.360	0.870
	run 3	0.277	0.349	0.795	0.299	0.361	0.826
	mean	0.245	0.354	0.692	0.286	0.364	0.786
	std	0.034	0.005	0.106	0.035	0.006	0.108
	range	0.068	0.010	0.212	0.066	0.012	0.206
20836	run 1	0.279	0.371	0.752	0.219	0.391	0.561
	run 2	0.255	0.372	0.686	0.269	0.379	0.710
	run 3	0.263	0.371	0.708	0.256	0.382	0.669
	mean	0.266	0.372	0.715	0.248	0.384	0.647
	std	0.012	0.001	0.034	0.026	0.006	0.077
	range	0.024	0.001	0.066	0.050	0.012	0.150
23812	run 1	0.247	0.374	0.661	0.280	0.380	0.737
	run 2	0.261	0.377	0.693	0.262	0.378	0.693
	run 3	0.229	0.382	0.599	0.273	0.373	0.731
	mean	0.246	0.377	0.651	0.271	0.377	0.721
	std	0.016	0.004	0.048	0.009	0.003	0.024
	range	0.033	0.008	0.095	0.018	0.007	0.044
26788	run 1	0.255	0.383	0.666	0.263	0.391	0.672
	run 2	0.265	0.378	0.700	0.292	0.386	0.757
	run 3	0.257	0.380	0.676	0.269	0.391	0.689
	mean	0.259	0.380	0.681	0.275	0.389	0.706
	std	0.005	0.003	0.018	0.015	0.003	0.045
	range	0.010	0.005	0.034	0.029	0.005	0.085
29765	run 1	0.254	0.388	0.655	0.275	0.394	0.699
	run 2	0.266	0.387	0.689	0.269	0.394	0.683
	run 3	0.262	0.388	0.676	0.265	0.395	0.670
	mean	0.261	0.388	0.673	0.270	0.394	0.684
	std	0.006	0.001	0.017	0.005	0.001	0.014
	range	0.012	0.002	0.034	0.010	0.002	0.029
32742	run 1	0.273	0.387	0.704	0.266	0.393	0.677
	run 2	0.271	0.389	0.696	0.263	0.390	0.675
	run 3	0.259	0.386	0.671	0.260	0.393	0.662

...continued on next page

Table B.8
(continued from previous page) Reynolds number test case II: $h_{0.7}/\bar{c} = 2.0$, $S_t = 0.3$, $\alpha_{max} = 15.0$.

R_e		C_T	C_P	η	C_T	C_P	η
	mean	0.268	0.388	0.690	0.263	0.392	0.671
	std	0.007	0.002	0.017	0.003	0.002	0.008
	range	0.014	0.003	0.033	0.005	0.003	0.014
35718	run 1	0.255	0.391	0.654	0.270	0.393	0.688
	run 2	0.256	0.391	0.656	0.261	0.393	0.662
	run 3	0.258	0.394	0.654	0.255	0.393	0.650
	mean	0.257	0.392	0.655	0.262	0.393	0.667
	std	0.001	0.002	0.001	0.007	0.001	0.019
	range	0.002	0.003	0.002	0.015	0.001	0.037

Table B.9
Reynolds number test case III: $h_{0.7}/\bar{c} = 1.5$, $S_t = 0.6$, $\alpha_{max} = 35.1$.

		smooth			tubercle		
R_e		C_T	C_P	η	C_T	C_P	η
11906	run 1	1.592	3.989	0.399	1.505	3.870	0.389
	run 2	1.525	3.997	0.382	1.485	3.884	0.383
	run 3	1.590	3.990	0.398	1.564	3.864	0.405
	mean	1.569	3.992	0.393	1.518	3.872	0.392
	std	0.038	0.004	0.010	0.041	0.010	0.011
	range	0.067	0.008	0.017	0.079	0.020	0.022
14882	run 1	1.609	4.100	0.393	1.520	4.027	0.377
	run 2	1.573	4.089	0.385	1.558	4.024	0.387
	run 3	1.558	4.096	0.380	1.491	4.055	0.368
	mean	1.580	4.095	0.386	1.523	4.035	0.377
	std	0.027	0.006	0.006	0.034	0.017	0.010
	range	0.052	0.011	0.012	0.067	0.031	0.019
17859	run 1	1.638	4.169	0.393	1.550	4.098	0.378
	run 2	1.628	4.160	0.391	1.542	4.099	0.376
	run 3	1.611	4.162	0.387	1.539	4.089	0.376
	mean	1.626	4.164	0.390	1.544	4.095	0.377
	std	0.013	0.005	0.003	0.006	0.005	0.001
	range	0.026	0.009	0.006	0.011	0.010	0.002
20836	run 1	1.662	4.208	0.395	1.550	4.128	0.376
	run 2	1.662	4.229	0.393	1.538	4.122	0.373
	run 3	1.630	4.215	0.387	1.562	4.120	0.379
	mean	1.652	4.218	0.392	1.550	4.123	0.376
	std	0.018	0.011	0.004	0.012	0.004	0.003
	range	0.032	0.021	0.008	0.024	0.008	0.006
23812	run 1	1.647	4.231	0.389	1.550	4.176	0.371
	run 2	1.605	4.241	0.378	1.538	4.169	0.369
	run 3	1.606	4.243	0.378	1.556	4.181	0.372
	mean	1.619	4.238	0.382	1.548	4.176	0.371
	std	0.024	0.007	0.006	0.009	0.006	0.002
	range	0.043	0.012	0.011	0.018	0.011	0.003
26788	run 1	1.618	4.239	0.382	1.537	4.174	0.368
	run 2	1.599	4.241	0.377	1.548	4.190	0.369
	run 3	1.636	4.222	0.388	1.544	4.186	0.369

...continued on next page

Table B.9
(continued from previous page) Reynolds number test case III: $h_{0.7}/\bar{c} = 1.5$, $S_t = 0.6$, $\alpha_{max} = 35.1$.

R_e		C_T	C_P	η	C_T	C_P	η
	mean	1.618	4.234	0.382	1.543	4.183	0.369
	std	0.019	0.011	0.005	0.005	0.009	0.001
	range	0.038	0.019	0.011	0.011	0.017	0.001
29765	run 1	1.611	4.225	0.381	1.540	4.211	0.366
	run 2	1.595	4.224	0.378	1.542	4.184	0.368
	run 3	1.599	4.223	0.379	1.527	4.188	0.365
	mean	1.602	4.224	0.379	1.536	4.194	0.366
	std	0.009	0.001	0.002	0.008	0.015	0.002
	range	0.016	0.001	0.004	0.015	0.027	0.004

Table B.10
Reynolds number test case IV: $h_{0.7}/\bar{c} = 2.0$, $S_t = 0.6$, $\alpha_{max} = 35.1$.

		smooth			tubercle		
R_e		C_T	C_P	η	C_T	C_P	η
11906	run 1	1.499	3.839	0.390	1.418	3.733	0.380
	run 2	1.587	3.830	0.414	1.368	3.740	0.366
	run 3	1.511	3.833	0.394	1.349	3.761	0.359
	mean	1.532	3.834	0.400	1.378	3.744	0.368
	std	0.048	0.004	0.013	0.036	0.015	0.011
	range	0.088	0.008	0.024	0.069	0.028	0.021
14882	run 1	1.548	3.908	0.396	1.401	3.907	0.358
	run 2	1.522	3.921	0.388	1.431	3.890	0.368
	run 3	1.466	3.923	0.374	1.424	3.900	0.365
	mean	1.512	3.917	0.386	1.418	3.899	0.364
	std	0.042	0.008	0.011	0.016	0.008	0.005
	range	0.082	0.014	0.022	0.030	0.017	0.009
17859	run 1	1.506	3.976	0.379	1.460	3.943	0.370
	run 2	1.504	3.977	0.378	1.430	3.935	0.363
	run 3	1.490	3.977	0.375	1.486	3.931	0.378
	mean	1.500	3.977	0.377	1.459	3.937	0.371
	std	0.009	0.001	0.002	0.028	0.006	0.007
	range	0.016	0.002	0.004	0.056	0.012	0.015
20836	run 1	1.513	4.025	0.376	1.444	3.990	0.362
	run 2	1.545	4.001	0.386	1.472	3.993	0.369
	run 3	1.518	4.004	0.379	1.435	3.988	0.360
	mean	1.525	4.010	0.380	1.450	3.990	0.363
	std	0.017	0.013	0.005	0.019	0.002	0.005
	range	0.032	0.025	0.010	0.037	0.005	0.009
23812	run 1	1.528	4.040	0.378	1.458	4.015	0.363
	run 2	1.510	4.048	0.373	1.437	4.009	0.358
	run 3	1.542	4.033	0.382	1.434	4.012	0.357
	mean	1.527	4.040	0.378	1.443	4.012	0.360
	std	0.016	0.008	0.005	0.013	0.003	0.003
	range	0.033	0.015	0.009	0.024	0.005	0.006
26788	run 1	1.519	4.035	0.376	1.463	4.052	0.361
	run 2	1.535	4.066	0.377	1.462	4.048	0.361
	run 3	1.524	4.056	0.376	1.488	4.044	0.368

...continued on next page

Table B.10
(continued from previous page) Reynolds number test case IV: $h_{0.7}/\bar{c} = 2.0$, $S_t = 0.6$, $\alpha_{max} = 35.1$.

R_e		C_T	C_P	η	C_T	C_P	η
	mean	1.526	4.052	0.376	1.471	4.048	0.363
	std	0.008	0.016	0.001	0.014	0.004	0.004
	range	0.016	0.030	0.002	0.025	0.008	0.007
29765	run 1	1.530	4.082	0.375	1.471	4.075	0.361
	run 2	1.530	4.090	0.374	1.473	4.082	0.361
	run 3	1.526	4.087	0.373	1.455	4.077	0.357
	mean	1.529	4.086	0.374	1.466	4.078	0.360
	std	0.002	0.004	0.001	0.010	0.004	0.002
	range	0.004	0.009	0.001	0.018	0.007	0.004

Bibliography

[1] J. M. Anderson, K. Streitlien, D. S. Barrett, and M. S. Triantafyllou. Oscillating foils of high propulsive efficiency. *Journal of Fluid Mechanics*, 360:41–72, 1998.

[2] D. N. Beal, F. S. Hover, M. S. Triantafyllou, J. C. Liao, and G. V. Lauder. Passive propulsion in vortex wakes. *Journal of Fluid Mechanics*, 549:385–402, August 2006.

[3] David Nelson Beal. *Propulsion through Wake Synchronization using a Flapping Foil*. PhD thesis, Massachusetts Institute of Technology, 2003.

[4] R. K. Edel and H. E. Winn. Observations on underwater locomotion and flipper movement of the humpback whale *megaptera novangilae*. *Marine Biology*, 48:279–287, 1978.

[5] F. E. Fish and J. M. Battle. Hydrodynamic design of the humpback whale flipper. *Journal of Morphology*, 225:51–60, 1995.

[6] Melissa Dawn Flores. Flapping motion of a three-dimensional foil for propulsion and maneuvering of underwater vehicles. Master's thesis, Massachusetts Institute of Technology, 2003.

[7] P. Freymuth. Propulsive vortical signature of plunging and pitching airfoils. *AIAA Journal*, 26:881–883, 1988.

[8] J. H. W. Hain, G. R. Carter, H. D. Kraus, C. A. Mayo, and H. E Winn. Feeding behavior of the humpback whale, *megaptera novaeangilae*, in the western north atlantic. *Fish. Bull.*, 80:259–268, 1982.

[9] Sighard F. Hoerner. *Fluid Dynamic Lift*. Hoerner Fluid Dynamics, Bakersfield, CA, 2nd edition, 1985.

[10] F. S. Hover, O. Haugsdal, and M. S. Triantafyllou. Effect of angle of attack profiles in flapping foil propulsion. *Journal of Fluids and Structures*, 19:37–47, 2004.

[11] C. M. Jurasz and V. P Jurasz. Feeding modes of the humpback whale, megaptera novangilae, in southeast alaska. *The Scientific Reports of the Whales Research Institute*, 31:69–83, 1979.

[12] A. Levshin, D. Custodio, C. Henoch, and H. Johari. Effects of leading edge protuberances on airfoil performance. *AIAA Paper*, 2006-2868, June 2006.

[13] J. C. Liao, D. N. Beal, G. V. Lauder, and M. S. Triantafyllou. The kàrmàn gait: novel body kinematics of rainbow trout swimming in a vortex street. *Journal of Experimental Biology*, 206:1059–1073, 2003.

[14] Stephen Licht, Victor Polidoro, Melissa Flores, Franz S. Hover, and Michael S. Triantafyllou. Design and projected performance of a flapping foil auv. *IEEE Journal of Oceanic Engineering*, 29(3):786–794, July 2004.

[15] Keith K. L. Lim. Hydrodynamic performance and vortex shedding of a biologically inspired three-dimensional flapping foil. Master's project, Massachusetts Institute of Technology, Department of Ocean Engineering, February 2005.

[16] Karl-Magnus Weidmann McLetchie. Force and hydrodynamic efficiency measurements of a three-dimensional flapping foil. Master's project, Massachusetts Institute of Technology, Department of Ocean Engineering and Department of Mechanical Engineering, May 2004.

[17] D. S. Miklosovic, M. M. Murray, L. E. Howle, and F. E. Fish. Leading edge tubercles delay stall on humpback whale (*megaptera novaeangliae*) flippers. *Physics of Fluids*, 16(5):L38–L42, 2004.

[18] David S Miklosovic, Mark M. Murray, and Laurens E. Howle. Experimental evaluation of sinusoidal leading edges. *Journal of Aircraft*, 44(4):1404–1407, July-August 2007.

[19] M. M. Murray, D. S. Miklosovic, F. E. Fish, and L. E. Howle. Effects of leading edge tubercles on a representative whale flipper model at various sweep angles. In *Proc. 14th UUST*, Durham New Hampshire, August 2005. AUSI.

[20] V. Polidoro. Flapping foil propulsion for cruising and hovering autonomous underwater vehicles. Master's project, Massachusetts Institute of Technology, Department of Ocean Engineering, June 2003.

[21] P. Prempraneerach, F. S. Hover, and M. S. Triantafyllou. The effect of chordwise flexibility on the thrust and efficiency of a flapping foil. In *Proc. 13th UUST*, Durham New Hampshire, August 2003.

[22] D. A. Read. Oscillating foils for propulsion and maneuvering of ships and underwater vehicles. Master's thesis, Massachusetts Institute of Technology, 2000.

[23] D. A. Read, F. S. Hover, and M. S. Triantafyllou. Forces on oscillating foils for propulsion and maneuvering. *Journal of Fluids and Structures*, 17:163–183, 2003.

[24] Phil Watts and Frank E. Fish. The influence of passive, leading edge tubercles on wing performance. In *Proc. 12th UUST*, Durham, New Hampshire, August 2001. AUSI.

[25] Becky L. Woodward, Jeremy P. Winn, and Frank E. Fish. Morphological specializations of baleen whales associated with hydrodynamic performance and ecological niche. *Journal of Morphology*, 267:1284–1294, October 2006.